THE EFFECTS OF SALINITY AND POLYMERS ON TRANSPORT OF IRON OXIDE NANOPARTICLES IN CONSOLIDATED CORES

Thesis

Submitted by

Jae Jin (Lisa) Han

In partial fulfillment of the requirements for the degree of

Master of Science

In

Civil and Environmental Engineering

TUFTS UNIVERSITY

August 2017

THESIS COMMITTEE:

Professor Kurt Pennell, Adviser (Tufts University)

Research Assistant Professor Bonnie Marion (Tufts University)

Research Professor John Germaine (Tufts University)

Abstract

The unique properties of nanomaterials have enticed many scientists to investigate the use of super-paramagnetic iron oxide nanoparticles (IO NPs) for enhanced oil recovery. While many transport studies have been conducted in unconsolidated media, transport behavior in consolidated media remains to be understood. In this work, laboratory-scale experiments were conducted to evaluate the transport behavior of IO NPs through Berea sandstone cores under varying experimental conditions (i.e. temperature, polymer preflood, filtering, salinity, electrolyte species, and concentration). The experiments, conducted with different background electrolyte solutions, revealed that ionic strength has a greater impact on IO NP transport than the presence monovalent vs. divalent cations. A limiting or maximum retention capacity, which has been observed in unconsolidated column studies, was also demonstrated in Berea sandstone when the input concentration of IO NP was increased from 100 to 1000 mg/L. The ability of polymers to serve as sacrificial site-blocking agents in Berea cores was confirmed based on the improved mobility of IO NPs following hydroxyethyl cellulose (HEC-10) preflood. This work provides experimental data that can be employed to improve down-hole delivery of nanomaterials for reservoir characterization, and to support the development and validation of predictive models for field-scale applications. Although this study focuses on IO NPs as contrast agents for use in subsurface reservoirs, the findings could be relevant for other types of NPs and other applications, such as imaging of salt-water impacted aquifers or in cases where iron NPs (e.g., zero valent iron) are used for environmental remediation.

Acknowledgements

This research was funded by the Advanced Energy Consortium (AEC). Member companies include Shell, Total, Statoil, Repsol, ExxonMobil, and BHP Billiton. From their mission statement, the consortium's primary goal is to develop intelligent subsurface micro and nanosensors that can be injected into oil and gas reservoirs to help characterize the space in three dimensions and improve the recovery of existing and new hydrocarbon reserves. Thank you to the AEC for sponsoring my graduate research under grant no. PV6234 and allowing me to improve my understanding of transport in the subsurface as it applies to both environmental contamination and energy development.

I would like to thank my thesis committee members; Professors Kurt Pennell, Bonnie Marion, and Jack Germaine. Kurt has been an incredible advisor and principal investigator for this project. I am very thankful to him for giving me the opportunity to join an amazing collaboration team at Tufts and the larger AEC family that conducts exciting research. Bonnie has been an amazing mentor and advisor throughout my Master's degree program. She has been incredibly patient in training me on column experiments and all the methods of analysis. Bonnie continued to support my research endeavors even during her hike across the Pacific Crest Trail. Jack has been an incredible mentor who has helped me develop the intact core system extensively used in this study. Thank you to Dr. Linda Abriola and her students for their modeling contributions to our research efforts. Thank you to Hamed Mohammadnejad for his continuous help in understanding various transport phenomenon observed in our experiments. Lastly thanks to Professor Keith Johnston's (University of Texas at Austin) contributions for his group's synthesis of the nanoparticles.

I would also like to thank everyone in the Pennell lab group. Working together in the lab and office has made even obstacles encountered in research quite enjoyable. I'd also like to thank my parents, my brother – Richard, and all my friends who have made my graduate experience very special and always full of love.

Table of Contents

List of Figures

List of Tables

Chapter 1: Introduction

By 2040, it is predicted that there will be 1.8 billion more people worldwide with a total population of 9 billion people (ExxonMobil 2017). The most significant implication of such an increase in population is the resulting stress on natural resources and increase in energy demand. The global energy demand is anticipated to increase by 25% from 2017 to 2040 (ExxonMobil 2017). According to the United States Energy Information Administration (EIA), countries within the Organization for Economic Cooperation and Development (OECD) account for 17% of the increase in energy demand for 2040 while non OECD countries contribute 90% (E.I.A. 2013). It is clear that the projected energy demand is driven by developing countries, and OECD countries reducing energy consumption will not negate the growing pressure for energy. Oil will remain the primary energy source, meeting one-third of the global energy demand by 2040 (ExxonMobil 2017), and improvement in oil recovery rates and overall reservoir management will be crucial in meeting the projected increase in energy demand among developing countries.

Roughly 32 billion barrels of fossil fuels are produced per year in the world (Sheng 2011). In order to sustain current levels of production, continuous new discoveries of oil reservoirs will have to be made, which is unlikely due to the finite nature of natural resources, or more efficient methods will need to be developed to produce oil and gas from known reservoirs. Furthermore, new discoveries are likely to be found in offshore, deep offshore, or in difficult-to-produce areas, which are often more expensive than producing from existing oil reservoirs using enhanced oil recovery (EOR) methods (Sheng 2011). EOR, also known as tertiary recovery, utilizes various techniques to increase the amount of oil that can be extracted from a reservoir. Common EOR methods include chemical (i.e., surfactant and/or cosolvent) flooding, thermal treatment, and miscible displacement with carbon dioxide, hydrocarbon or nitrogen injection

(Mid-Con Energy Partners, LP. 2014). Up to 1993, a total of 536 billion barrels of oil was discovered with the total produced being 162 billion barrels (30% of the total discovered) and the reserves being 23 billion barrels (Sheng 2011). That leaves 351 billion barrels of oil remaining in the reservoirs or 66% of the total discovered. If EOR can recover half of the remaining oil, the currently projected recoverable reserves (162 billion barrels) can be doubled (Sheng 2011). It is therefore crucial to advance research in EOR to ensure a readily available supply of oil for decades to come.

One example of EOR involves the application of engineered nanoparticles. Nanoparticles can be defined as particles with at least one dimension less than 100 nm. For the purposes of this study, a broader definition of "nano", dimensions in the range of 100-1000 nm, will be used. The unique properties of nanomaterials such as lightness in weight, corrosion resistance, and mechanical strength (Matteo, Candido et al. 2012) have been exploited for various uses in the oil industry. Research efforts have been made to couple superparamagnetic nanoparticles and an external magnetic field for improved reservoir characterization (Prodanovic et al., 2010; Ryoo et al., 2012), employing the concept of magnetic resonance imaging. Nanoparticles have also been evaluated as mobility control agents for highly viscous oil (Zhang et al. 2010), as well as conformance control and mobility control agents for CO_2 flooding (Espinosa et al. 2010). Further understanding the transport properties of these engineered nanoparticles under varying reservoir conditions is required to advance nanomaterial applications for reservoir characterization.

Several nanoparticle mobility studies have been conducted in unconsolidated media (Kmetz et al. 2016, Li et al. 2008, and Xue et al. 2014), which have revealed transport behavior of nanoparticles in the presence of polymers and surfactants, under varying flow conditions, and grafted copolymer composition, respectively. Due to the associated complexity of performing

nanoparticle mobility tests in consolidated cores, transport studies in intact sandstone cores (e.g., Berea) have not been investigated extensively. With 22 out of the 32 billion barrels of oil produced each year coming from sandstone reservoirs (Sheng 2011), it is crucial to extend our understanding of nanoparticle mobility in consolidated sandstones.

1.1 Research Purpose

The overall objective of this work was to evaluate the mobility of iron oxide nanoparticles (IO NPs) through consolidated sandstone cores under varying experimental conditions in order to understand the mechanisms controlling IO NP mobility. The results of this work can inform the development and validation of mathematical models designed to predict nanoparticle mobility at larger scales.

1.2 Research Goals

1. Determine the impact of salinity, input concentration, and straining on the mobility of IO NPs through intact Berea sandstone cores.
    a. Hypothesis: IO NP retention will increase with increased salinity of the background electrolyte due to NP aggregation and strong attachment on mineral surfaces. IO NP retention will also increase with increased nanoparticle concentration as increases in NP concentration have shown to increase aggregation. Straining will inhibit larger particles from mobilizing through the core.

b. Research Approach: Perform column studies and measure IO NP concentrations in effluent breakthrough curves and solid-phase retention profiles. To evaluate the effect of salinity on IO NP mobility: conduct column studies with API (American Petroleum Institute) brine (8 wt. % Sodium Chloride, 2 wt. % Calcium Chloride) and compare to column experiments conducted under lower salinity conditions - 500 mg/L sodium chloride (NaCl) background and 2M NaCl (equivalent ionic strength to the API brine). To evaluate the effect of applied concentration on IO NP mobility: conduct one column with an injection concentration of 1,000 mg/L IO NPs and compared to another column run at 100 mg/L IO NPs (but with the same total IO NP mass injected). To evaluate the effect of straining on IO NP mobility: evaluate the hydrodynamic size of the IO NP suspension influent and effluent via DLS-size measurements.

2. Determine the mobility of IO NPs in Berea sandstone following a polymer preflood.
    a. Hypothesis: A polymer preflood will enhance IO NP mobility due to blocking of surface attachment sites.
    b. Research Approach: Perform intact core flood experiments with and without a polymer (1,000 mg/L hydroxyethyl cellulose, HEC-10) preflood. A column experiment with polymer preflood conducted with 1,000 mg/L IO NPs in API brine will be compared to a column experiment conducted without polymer preflood but with the same IO NP concentration and background solution.
3. Determine the impact of temperature on the mobility of IO NPs through Berea sandstone.

a. Hypothesis: IO NP retention will increase at elevated temperatures due to increased energy of NPs and the resulting reduced energy barrier for adsorption.
b. Research Approach: Conduct column experiments at room temperature and another column at 50˚C.A column experiment conducted at 50˚C with 1000 mg/L IO NPs in API brine will be compared to a column experiment conducted at room temperature (22˚C) with the same IO NP concentration and background solution.

4. Develop and test a screening apparatus to rapidly evaluate new nanoparticle formulations and the impact of experimental parameters on nanoparticle mobility and face plugging (straining) behavior.
    a. Hypothesis: The inlet faces of the sandstone discs from the screening test under varying conditions will display similar retention behavior as the respective inlet faces of the Berea sandstone cores run in intact core experiments.
    b. Research Approach: Deliver IO NP solution (IO NPs in API brine, IO NPs in API brine with HEC-10 preflood, IO NPs in 500 ppm NaCl) to the inlet face of intact sandstone disc of the screening apparatus to observe retention behavior at the face.

Chapter 2: Literature Review

2.1 Nanoparticle Applications

The promising functionalities of nanomaterials have been exploited in a variety of disciplines from medical applications to automotive, textile, and energy. In medicine, nanotechnology is being investigated for delivery and release of drugs to specific locations in the body to provide more focused and effective treatments. Sershen et al. (2000) designed gold nanoshells to absorb near-infrared light to initiate temperature change and enhance drug release. The ability to manipulate the size of the core and shell of these gold nanoshells has been the key to optimizing light absorption (Sershen et al., 2000). Nanoparticles are also employed as contrast agents in the field of medicine to reveal the mechanisms of disease processes and the effects of therapy. They have noteworthy advantages over single molecule-based contrast agents including: producing excellent contrast, integrating multiple properties such as several types of contrast generating materials, lengthy circulation time, and carrying high payloads (Cormode et al., 2008). Magnetic nanoparticles have the additional advantage of magnetic responsiveness and magnetic resonance imaging (MRI) visibility (Chertok et al., 2008). Several investigators have demonstrated that magnetic nanoparticles can be retained at tumor sites with local administration and a locally applied external magnetic field (Pulfer et al., 1999 and Alexiou et al., 2003). With increasingly strict environmental regulations, the automotive industry has used cerium oxide nanoparticles, taking advantage of the high surface-to-volume ratio of nanoparticles compared to conventional powders, as fuel additives on biodiesel to reduce fuel consumption and toxic emissions (Sajith et al. 2010). The textile industry, one of the initial adopters of nanotechnology, has incorporated nanoparticles into their process innovation to obtain lower unit costs, larger capacity, and better quality (Matteo, Candido et al. 2012).

In 2008, the Advanced Energy Consortium (AEC) was founded in cooperation with major oil companies such as BP, ConocoPhillips, Shell, Total and Schlumberger to tap into the potential of nanotechnology (Matteo, Candido et al. 2012). Funded by the AEC, Oklahoma University has published work on Single-Walled-Carbon-Nano Tube (SWNT)/Silica nanohybrids, which react and modify the oil properties to increase oil mobility when delivered to an oil/water interface (Villamizar et al. 2010). Another application of nanotechnology in the oil industry has been the development of sensors and imaging-contrast agents. Nanomaterials ("smart fluids") can be injected downhole as high resolution sensors for temperature, pressure and stress under harsh reservoir conditions (Matteo, Candido et al. 2012). Described as "slightly" smart nanosensors, nanoparticles 100-1000 nanometer (nm) in diameter could be injected through pores of reservoir media to analyze the formation characteristics. While there will be no active components such as sensors, data storage and transmission, the unique interactions of the nanoparticles with the reservoir could reveal threshold data including temperature, pressure, pH, and salinity (Matteo, Candido et al. 2012). Yu et al. (2010) observed that both pH and salinity control the electrostatic repulsion between the particles and between the particle and pore wall from their transport studies of surface-treated paramagnetic IO NPs in Boise sandstone (480 mD) and layered Berea sandstone (86 mD) cores. Temperature and pressure sensitive nanomaterials have been recognized as a potential method to reveal fracture connectivity and geometry in reservoir rocks (Mohammed et al., 2010). Mohammed et al. (2010) conducted preliminary tests to assess parameters involved in nanoparticle mobility such as particle size and shape, surface charge, and affinity to rock for this application. Nanoparticles can be employed to determine the size of the reservoir fractures by analyzing the change in particle size distribution of the nanoparticles injected and recovered from wells (Mohammed et al., 2010). The magnetic

susceptibility of superparamagnetic iron oxide nanoparticles has also been evaluated as a means to monitor transport behavior through a reservoir using magnetic sensors. Prodanovic et al. (2010) and Ryoo et al. (2012) have demonstrated that paramagnetic nanoparticles have the capability of displacing the oil-water interface under the influence of an external magnetic field. The use of superparamagnetic IO NPs for improved reservoir characterization will be the focus of this proposal.

2.2 Magnetism and Subsurface Applications

Maghemite (γ-Fe_2O_3), Hematite (α-Fe_2O_3), and Magnetite (Fe_3O_4) are among the most common forms of iron oxides that exist in nature. Maghemite is found in soils as a weathering product of magnetite or as a product of heating of other iron oxides. Hematite is the oldest known of the iron oxides and is found in rocks and soils. Magnetite, also known as black iron oxide, magnetic iron core, lodestone, or Hercules stone has the strongest magnetism of any transition metal oxide (Teja and Koh 2009). The abundance, magnetic susceptibility, and relatively low toxicity of magnetite make it an ideal choice for subsurface characterization.

Magnetic fluids have been utilized for decades in a variety of applications including sealing, damping, heat transfer, bearing, and sensing/detection. Ferrofluids, a commercially available magnetic liquid, has widely been applied to various applications since the founding of Ferrofluidics Corporation in 1966 (Raj and Moskowitz 1990). This magnetic liquid is a stable colloidal suspension of ferromagnetic particles that are covered with a molecular layer of dispersant. While Brownian motion keeps the particles in suspension, the layer of dispersant keeps the particles from aggregating (Moridis et al. 2001). The first ferrofluid product to be

developed and commercialized was a dynamic process seal. The seal used electric circuits to apply a strong magnetic field to allow the ferrofluid to act as uncompromising O-rings around a rotating shaft (Raj and Moskowitz 1990). In the textile industry, ferrofluidic seals are employed as barriers for the motor bearings from the fibrous contaminants in the environment to ensure a longer bearing life (Raj and Moskowitz 1990). Ferrofluids have also been used in nuclear magnetic resonance (NMR) probes to detect free and shale oil (Raj and Moskowitz 1990).With the stability of the ferrofluids from the dispersant layer, external magnetic fields and gravity cannot significantly alter the concentration of the magnetic particles in the carrier liquid. As a result, ferrofluids can move homogeneously with the influence of a magnetic field, and can be manipulated into any direction without any physical contact (Moridis et al. 2001). Moridis et al. (Moridis et al. 2001) have demonstrated that ferrofluids can be used to control liquid movement and can be utilized as tracers imaged by standard electromagnetic and geophysical methods. While ferrofluids are useful for many applications, a more stable and highly magnetically susceptible particle is needed for the harsh reservoir conditions that will be encountered in subsurface oilfield reservoirs (e.g. high salinity, heat, pH, and heterogeneous porous media).

Ryoo et al. (2012) validated the concept of detecting the acoustic response of in-house synthesized and surface-modified IO NPs after inducing a magnetic field. By measuring the air-ferrofluid interface motion with the phase-sensitive optical coherence tomography (PS-OCT), Ryoo et al. (2012) observed higher interfacial displacements with bigger nanoparticle cluster sizes with similar magnetization and with higher magnetization with similar cluster sizes. While paramagnetic particles have the advantage of reduced magnetic hysteresis (particles do not retain their magnetic moment once the field is removed), superparamagnetic particles have the additional advantage of higher magnetic susceptibility (Bean and Livingston 1959).

Superparamagnetism is achieved when the magnetic pole becomes large enough to be considered thermodynamically independent single-domain particles. These single-domain particles, called magnetic domains, contain a magnetic dipole that is larger than the sum of its individual unpaired electrons (Wang et al. 2001). In the absence of an induced magnetic field, these magnetic domains rotate freely from thermal motion and are oriented randomly. Once an external magnetic field is introduced, the magnetic dipoles of the magnetic domains reorient themselves similar to paramagnetic particles (Wang et al. 2001). Bean and Livingston (1959) recognized two requirements for superparamagnetism to occur: 1) the magnetization curve, which describes the relationship between the induced magnetic flux density and the magnetizing force, cannot display an hysteresis and 2) the magnetization curve for an isotropic sample must be temperature dependent (Bean and Livingston 1959).

2.3 Nanoparticle Stability and Transport

Stability is a key factor for successful implementation of nanoparticles for reservoir characterization due to the harsh environment of oil reservoirs (e.g., high salinities (>1 M ionic strength), presence of divalent salts (Ca^{2+} and Mg^{2+}), and high temperature (up to 150˚C) (Xue et al., 2014)). Wang et al. (2008) found that aggregation of fullerene nanoparticles was dependent on electrolyte species and concentration with more aggregation observed with increasing electrolyte concentration, especially in the presence of $CaCl_2$. The authors explained the observed aggregation behavior using the Derjaguin-Landau-Verwey-Overbeck (DLVO) theory, where the interaction energy between two particles is composed of the electrical double-layer repulsion energy and the van der Waals attraction energy (Verwey et al., 1948). In the presence

of $CaCl_2$, the interaction energy has a higher net attractive energy with increasing electrolyte concentration due to the strong suppression of the electrical double layer by divalent cations with van der Waals attractive forces dominating (Wang et al., 2008).

Other important considerations that can affect the transport behavior of nanoparticles is physical straining and calcium bridging. Straining occurs when the pore throat sizes between grains is not large enough to allow the passage of particles. Straining is considered to be important when the ratio of particle diameter to the grain diameter is greater than 0.0017 or 0.008 (Bradford et al., 2002; Xu et al., 2006). Physical straining is often cited as the cause of nanoparticle retention in porous media when a hyperexponential retention profile is observed (Li et al., 2008; Hong et al., 2009; Raychoudhury et al., 2014). Calcium bridging occurs when anionic functional groups bind to Ca^{2+} adsorbed by a negatively charged clay surface (Sposito, 2008). Retention of NPs is often attributed to this bridging complexation (Torkzaban et al., 2012; Xue et al., 2014). Torkzaban et al. (2012) found quantum dots deposited on clay surfaces of acid-treated Accusand via SEM imaging. A salt cleaning method was used to remove the clay from the acid-treated Accusand, which resulted in lower deposition of quantum dots and carboxylate-modified latex (CML) nanoparticles at varying Ca^{2+} concentrations. From these findings, Torkzaban et al. (2012) attributed the high deposition results of QDs and CML particles to the Ca^{2+} bridging complexation.

Synthesizing magnetite nanoparticles suitable for subsurface imaging is challenging due to the many crucial pre-requisites for this application: 1) ability to remain in suspension without aggregating, 2) ability to remain stable for long durations at high temperature and high-salinity conditions while traveling in the reservoir, and 3) mobility over a long distance in the reservoir with minimal retention (Yu et al. 2012). Polymers can be effectively used as stabilizers for

nanoparticles if the polymer itself is soluble in the solvent. However, polymers often suffer under typical oil reservoir conditions and will often precipitate or chemically deteriorate at high salinities and temperature. For example, high molecular weight polymer such as polyacrylamides (PAM) hydrolyzes at high temperatures and precipitates with divalent ions while weak polyelectrolytes such as poly(acrylic acid) (PAA) remains soluble at high temperature in 1 M NaCl but precipitates at room temperature in the presence of divalent Ca^{2+} (Xue et al. 2014).

Xue et al. (2014) studied the effect of a copolymer coating, poly(2-acrylamido-2-methyl-1-propanesulfonic acid-*co*-acrylic acid) or poly(AMPS-*co*-AA), a highly acidic polymers with higher calcium tolerance, on the stabilization and mobility of IO NPs in porous media. Using a 3:1 ratio of AMPS to AA, 96.0% mass breakthrough of IO NPs injected into a column of 40-50 mesh Ottawa Sand saturated with API brine (8% NaCl, 2% $CaCl_2$) was obtained (Xue et al. 2014). This was the first study to demonstrate mobility of IO NPs under such high salinity conditions (ionic strength = 1.9 M). To further explore the effect of electrolyte composition on the mobility of these poly(AMPS-co-AA) grafted IO NPs, two column studies were conducted with background solutions of 2.04 M NaCl and 0.68 M $CaCl_2$ (same total ionic strength as API brine) respectively (Xue et al. 2014).The authors observed 40% more retention of IO NPs to Ottawa sand for a background solution of 0.68 M $CaCl_2$ compared to 2.04 M NaCl. The increased retention was attributed to divalent cation (Ca^{2+}) inducing bridging and hydrophobic interactions (Xue et al. 2014). The work described in this thesis will also evaluate the effect of electrolyte species and concentration on nanoparticle transport to determine whether the observed transport behavior in consolidated media is consistent with DLVO theory.

In addition to modifying nanoparticle coatings, researchers have evaluated the use of co-injection or preflood polymers to enhance NP mobility. Kmetz et al. (2016) studied the effect

polymer use on IO NP transport through finer 60-170 mesh crushed Berea sandstone. With no polymer additives incorporated, injection of 2,500 mg/L IO NPs resulted in retention greater than 60%. When the same concentration of IO NPs was co-injected with 1,000 mg/L hydroxyethyl cellulose (HEC-10), the mobility increased two-fold (78% recovery), and co-injection with 1,000 mg/L gum arabic resulted in a slightly lower recovery of 72% (Kmetz et al. 2016). A preflood of 1,000 mg/L of HEC-10 prior to the injection of IO NPs resulted in an additional 20% improvement in mobility compared to when IO NPs was injected without a polymer preflood (Kmetz et al. 2016). Model validation of the experimental results confirmed the site-blocking mechanism of the polymers, which screened active attachment sites, allowing the IO NPs to move through the column with increased facility. The present study also evaluated the effect of a polymer preflood (HEC-10) on IO NP transport to determine whether if the site-blocking mechanism applies to the transport behavior in consolidated media.

While many previous studies have evaluated transport in unconsolidated porous media, it is important to evaluate transport through consolidated/intact cores, which are more representative of field conditions (22 out of the 32 billion barrels of oil produced each year come from sandstone reservoirs (Sheng 2011)). Yu et al. (2014) have conducted IO NP column studies using intact Boise sandstones cores (750-1000 mD) at lower salinity (0-1% wt. NaCl) compared to API brine (Yu et al. 2014). The authors demonstrated that when coated with a crosslinked polymer, their superparamagnetic IO NPs were able to mobilize through the Boise sandstone with little retention. The current study examined the transport behavior of IO NPs through Berea sandstone cores, which have a permeability of 198-248 mD (Thomas et al. 2012). Mohammed et al. (2012) investigated the effects of nanoparticle size and shape and surface charge in its mobility through Berea sandstone. The authors found that while Ag nanowires were trapped at

the inlet of the core, spherically shaped Ag nanoparticles with similar surface characteristics were able to flow through the sandstone at 25% recovery. They also observed an optimum particle size (200 nm and smaller) for the transport of Sn-Bi alloy nanoparticles through Berea sandstone and that the surface charge of the nanoparticles modified with surfactant improved mobility of the particles (Mohammed et al. 2012). In addition to the effects of pre-filtration to evaluate the effect of size on IO NP mobility, the work presented herein will evaluate transport behavior at a higher temperature (50˚C) and at different IO NP concentration in Berea sandstone. These core studies aim to support the development and application of superparamagnetic particles for subsurface characterization of oil reservoirs, which could reveal areas of fractures, highly transmissive channels, and low permeability zones.

Chapter 3: Experimental Approach and Methods

3.1 Nanoparticle Preparation

Iron oxide nanoparticles (IO NPs, magnetite, Fe_3O_4) were synthesized in the laboratory of Dr. Keith Johnston (University of Texas at Austin) following the procedures described by Muhammad et al. (2016). Synthesized in triethylene glycol (TEG) (Fisher Scientific, Waltham, MA), the magnetite particles used for this study consist of a new class of polymer grafted IO NPs with sizes smaller than 50 nm and low polydispersity. Briefly, 5 g of iron (II) acetate (Fisher Scientific, Waltham, MA) were dissolved in 50 mL of TEG, and the reaction mixture was purged with argon for 20 minutes before heating to 210 °C in 20 minutes. After 2 hours, the resulting IO NPs and excess TEG were diluted with ethanol and centrifuged at 10,000 rpm for 10 minutes and the pellet was redispersed in ethanol. This process was repeated three times to remove excess TEG. The IO NPs was purified via bath sonication in 1.3 pH hydrochloric acid (HCl) (Sigma-Aldrich, St. Louis, MO) solution for 10 min with ice followed by centrifugation with a mixture of ethanol and ethyl acetate at 10,000 rpm. The synthesized TEG functionalized IO NPs were then coated with silica, 3-aminopropyl triethoxysilane (APTES) (Sigma-Aldrich, St. Louis, MO) and finally grafted with a ratio of 3:1 of monomer 2-amino-2-methylpropanesulfonate (AMPS) (gift from Lubrizol corporation) to acrylic acid (Sigma-Aldrich, St. Louis, MO) as reported in Xue et al. (2014). This methodology optimized the need for particle stabilization and low adsorption/retention with AMPS, and the need for permanent attachment of the stabilizer with acrylic acid using a 3:1 AMPS to AA ratio as the copolymer (Xue et al. 2014).

3.2 Porous Media

Intact Berea sandstone cores (1 in dia. x 3 in length) were used to conduct the transport studies of IO NPs. Cores were obtained from Kocurek Industries (Caldwell, TX) and cut from five Berea sandstone blocks of 13" x 13" x 7" (Block 105, 106, 107, 108, and 109) by a commercial laboratory (Stim-Lab, a division of Core Laboratories Inc., Duncan, OK). Blocks 105, 106, and 108 were selected and sampled for quality testing (Thomas et al. 2012). The experiments presented here were conducted in cores cut from Block 109. X-ray diffraction (XRD) was used to determine the brine permeability (94.7 ± 9.67 mD), porosity (20%), surface area, and mineral composition at Stim-Lab. The XRD analysis of the Berea blocks is shown in Table 2. The specific surface area (SSA) of intact Berea sandstone is 1.5 m^2/g, and the median pore radius averaged 7.41 µm, which was obtained conducting high pressure mercury injection (HPMI). Permeability of the core ranges from 198 to 249 mD with an average of 223 mD and standard deviation of 20.41 (Thomas et al. 2012).

Table 1. XRD Analysis of Berea blocks. XRD were performed on both bulk and clay fractions and reported as weight percent composition (Thomas et al. 2012).

								*Swelling			
Sample Name	Quartz %	Plagioclase %	K-feldspar %	Calcite %	Ankerite %	Siderite %	Total Clays %	Illite %	Clay %	Chlorite %	Kaolinite %
Block 102	83	2	6	trace	2	trace	7	3	-	1	3
Block 103	83	2	5	trace	2	1	7	3	-	1	3
Block 104	82	3	6	trace	1	1	7	3	-	1	3
Block 105	87	2	5	trace	-	-	6	4	trace	-	2
Block 106	85	2	7	trace	-	-	6	3	trace	-	3
Block 108	88	2	5	trace	-	-	5	2	trace	-	3

3.3 Stabilizing Agents

Hydroxyethyl cellulose (HEC-10), purchased from Sigma-Aldrich (St. Louis, MO), was employed as the stabilizing agent to enhance IO NP mobility. HEC-10 is used as a viscosity modifier and stabilization agent in a variety of industries ranging from beauty products to oil and gas production.

3.4 Column Experiments

Nanoparticle mobility studies were conducted using Durable Polycarbonate Clear Tubing (1.25 in dia. X 3 in length) (McMaster-Carr, Elmhurst, IL), which held the intact Berea sandstone core. At the start of the core preparation, a plastic mesh was placed on top of the face on each side of the core. Duct tape was used to cover the ends of the core, securing the plastic mesh onto the face. The plastic mesh protects the face from direct contact with the duct tape, while the duct tape protects the face during core preparation. High Strength (2-ton) Epoxy (McMaster-Carr, Elmhurst, IL) was applied with a paint brush on the lateral sides of the Berea sandstone cores to prohibit flow through the lateral sides. Wrap-Tight Tubing (1.45”ID before shrinking, McMaster-Carr, Elmhurst, IL) was then placed around the middle of the epoxied intact sandstone with approximately half- inch of the expoxied sandstone not covered by the Wrap-Tight Tubing on each end, and heat was applied via a heat gun to allow the Wrap-Tight Tubing to fit tightly around the intact stone (Figure 1a). The heat shrink tubing allows the intact Berea sandstone to fit snugly into the polycarbonate tube (Figure 1b). The annular space in the polycarbonate tube not contained by the heat shrink tubing on each end was filled with high strength epoxy (Figure 1c). Any remaining space above the hardened high strength epoxy on

each end was filled with Dow Corning silicone sealant (McMaster-Carr, Elmhurst, IL) (Figure 1d).

Each end of the polycarbonate tube containing the epoxied Berea sandstone core was fitted with 1.25" PVC Compression Male Adapter (NDS, Lindsay, CA), Thick-wall dark gray Polyvinyl Chloride (PVC) pipe fitting (McMaster-Carr, Elmhurst, IL), Type 316 stainless steel threaded pipe fitting (1 Male x 1/4 Female, Hex Reducing Bushing) (McMaster-Carr, Elmhurst, IL) and Type 316 stainless steel Yor-Lok tube fitting (Straight Adapter for 1/8" Tube OD x ¼ NPT Male) (McMaster-Carr, Elmhurst, IL) in this respective order (Figure 2a). The ends of the intact core system had 1/8" Swagelok tube fitted with a 316 stainless steel ferrule (Swagelok, Solon, OH) to connect 1/8" polytetrafluoroethylene (PTFE) tubing to a female threaded opening which were connected to Hamilton 3-way valves (Figure 2b). The Hamilton valves were used to control inflow and outflow at both ends of the column. Each intact core fitting end held a 1/8" stainless steel pipe, and the annular space around the stainless steel pipe was filled with high strength epoxy (Figure 2c).The end of the stainless steel pipe and the surface of the hardened high strength epoxy were designed such that the face of the Berea sandstone would be placed directly against the end of the stainless steel pipe and hardened epoxy, delivering flow directly to inlet face of the Berea sandstone.

For core experiments run at elevated temperature (50˚C), the column apparatus was heated by wrapping silicone heat tape (1" wide x 2' long, BriskHeat, Columbus, OH) around the core apparatus and wrapping XtremeFLEX HTC flexible heating cord (3/16" diameter, 3' length) (BriskHeat, Columbus, OH) around the influent line. The temperature regulator for the heating cord was set at 50˚C, and the temperature regulator for the silicone heat tape was set at 52˚C to ensure the temperature does not exceed the temperature limits of each component in the

column apparatus. The column apparatus and influent line was covered with insulating material. The system was left to heat for 2.5 hours in order to reach 50˚C, which was determined from a preliminary experiment. In the preliminary experiment, one end of the column fittings was used to pack 40-50 mesh Ottawa Sand that contained a thermometer with the opening covered with tape. The column fittings were then wrapped with silicon heat tape, which was wrapped with insulating material.

In order to remove entrapped air, the dry intact core system was purged with an up-flow of pure CO_2 gas for at least 20 minutes prior to aqueous phase saturation. An effluent line was attached to the top of the intact core holder and placed into a beaker of deionized (DI) water to observe the slow and steady bubbling from the purging gas.

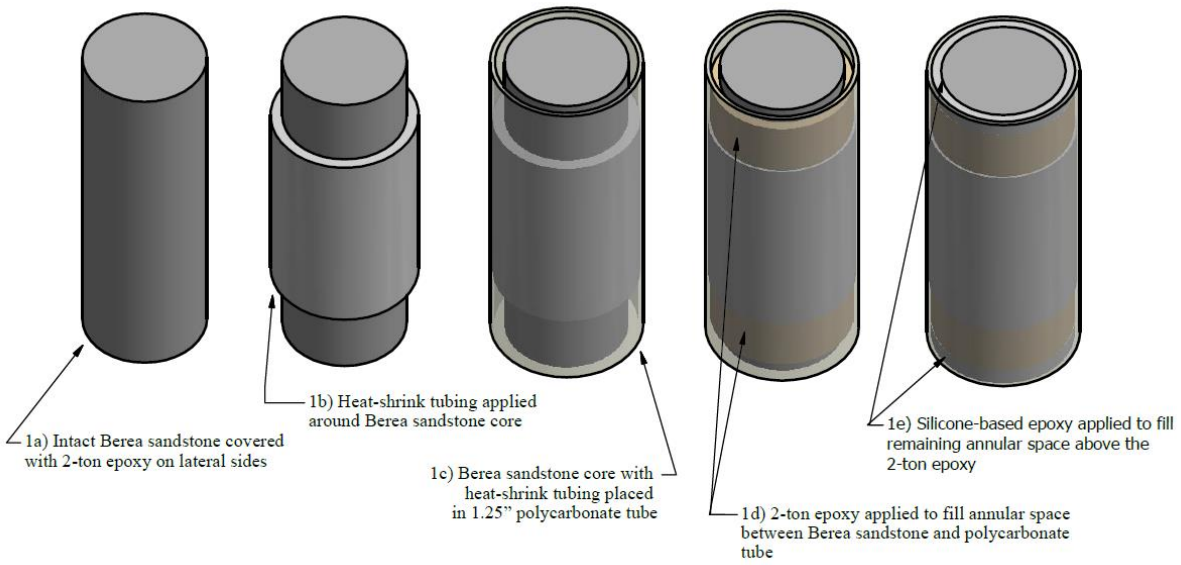

Figure 1. Figure of Berea sandstone intact core being prepared for column test.
Drawn by Jae Jin Han
5/13/17

Figure 1. a) Intact Berea sandstone covered with 2-ton epoxy on lateral sides. b) Heat shrink tubing placed applied around Berea sandstone core. c) Berea sandstone with heat shrink tubing placed in 1.25" polycarbonate tube. d) 2-ton epoxy applied to fill annular space between Berea sandstone core and polycarbonate tube on each end. e) Silicone-based epoxy applied to fill remaining annular space above the 2-ton epoxy on each end.

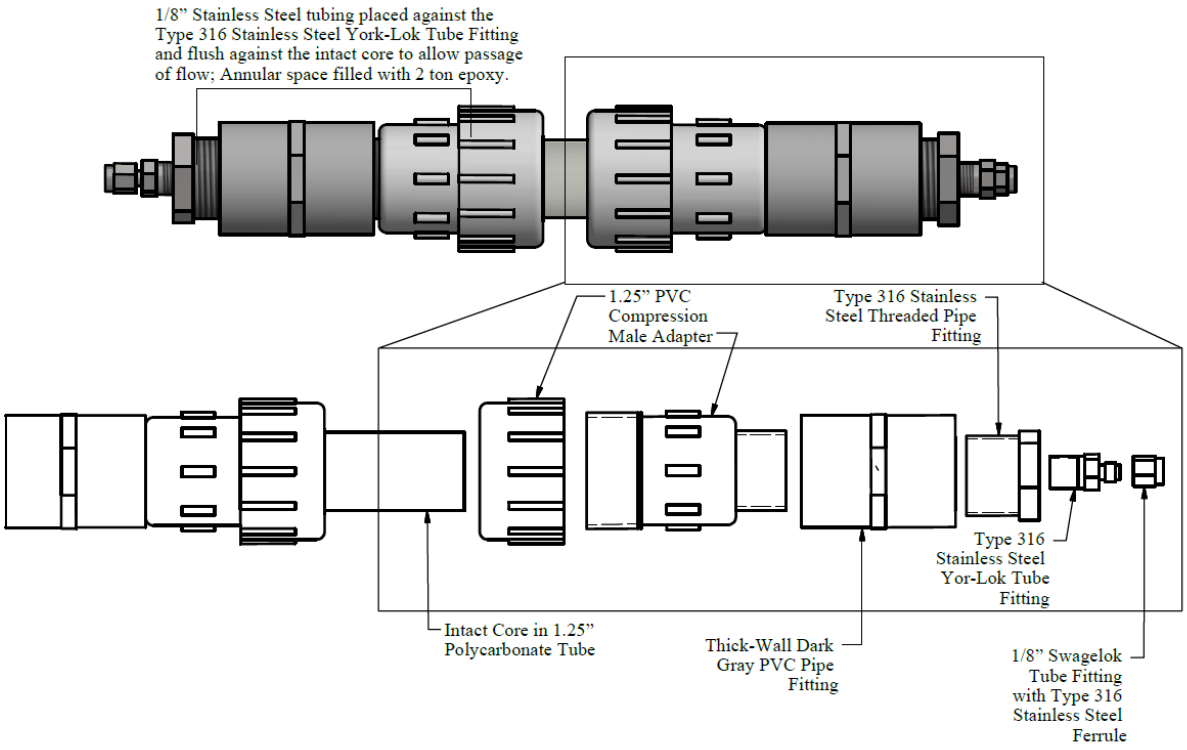

Figure 2. Figure of Intact Core System.
Drawn by Jae Jin Han
5/13/17

Figure 2. Intact core system. Fitting parts from bottom to top: 1.25" PVC Compression Male Adapter, Thick-Wall Dark Gray PVC Pipe Fitting, Type 316 Stainless Steel Threaded Pipe Fitting, Type 316 Stainless Steel Yor-Lok Tube Fitting, 1/8" Swagelok Tube Fitting with Type 316 Stainless Steel Ferrule to connect 1/8" plastic tubing to a female threaded opening, and 3-way Hamilton valve. High Strength Epoxy fills the annular space around the 1/8" stainless steel pipe.

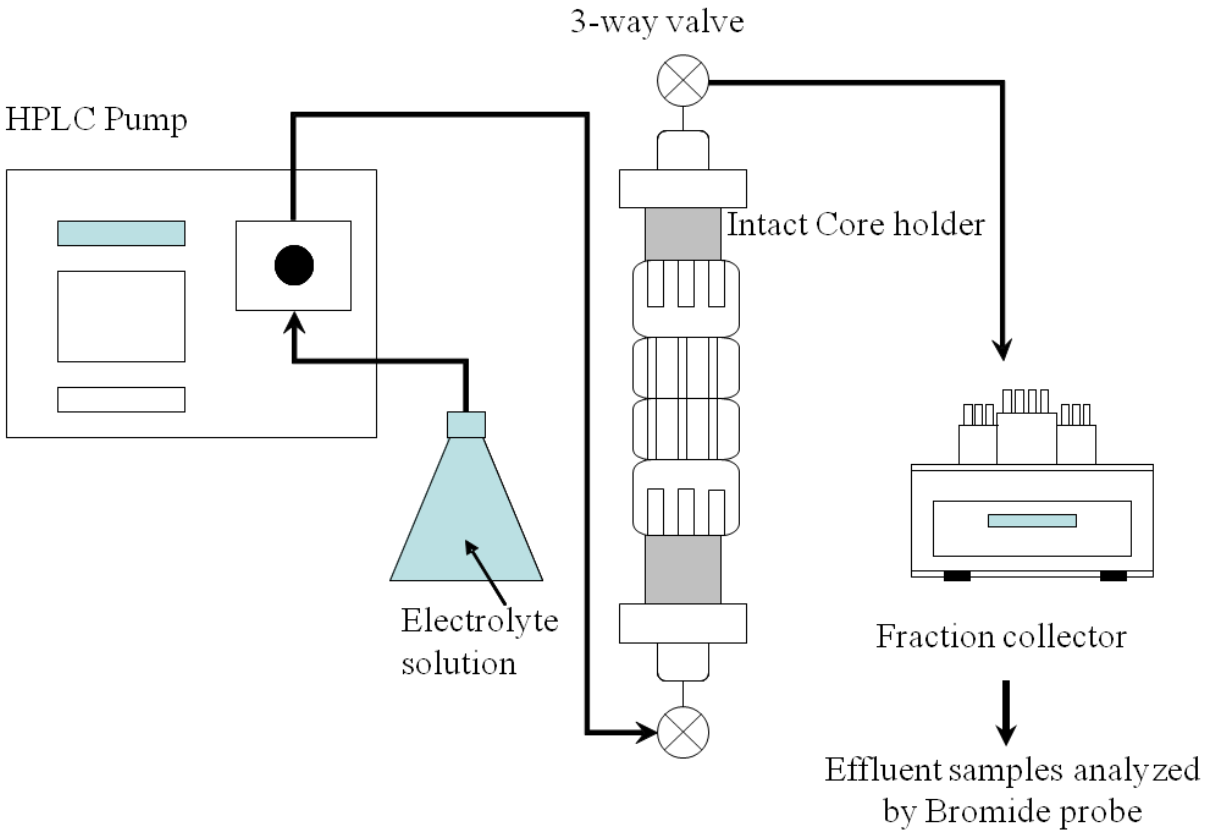

Figure modified from Bonnie Marion

Figure 3. Experimental set up of a column study. The electrolyte solution is injected via a HPLC pump into the column and flows in an up-flow direction. The effluent solution comes out at the top of the column and gets collected by a fraction collector.

The columns were then saturated in an up-flow direction with a background salt solution e.g., API brine, 8% wt. NaCl + 2% wt. $CaCl_2$ (IS = 2.0 M), prepared with degassed DI water using a Dynamax SD-200 pump (Varian Inc., Palo Alto, CA) outfitted with a 25-mL pump head and dampener. The saturation flow rate was set to 1.0 mL/min. The mass of the intact core system was determined before and after saturation to calculate the porosity (~0.25) and pore volume (~10 mL). After at least 10 pore volumes (PVs) of the background salt solution was injected, a nonreactive tracer (~3.5 PVs) was injected in an up-flow direction using a Series I

Pump (Chrom Tech Inc., Apple Valley, MN) to determine the hydrodynamic dispersion and overall flow of each column. A non-reactive tracer (NaBr) was injected at 1 mL/min or a pore-water velocity of approximately 12m/day. The concentration of sodium bromide used for the tracer test was selected to match the ionic strength of the background salt solution (i.e., 2.0 M solution of NaBr for API brine). After approximately 3.5 PVs of NaBr was injected into the saturated core, the HPLC pump was briefly paused and the injection solution was switched back to the background salt solution. The background salt solution was then injected for another 3.5 PVs. The re-introduction of the background salt solution allows the backside of the NaBr breakthrough concentration curve to be captured in the collected samples. Effluent samples from the core were collected in 15-mL sterile plastic centrifuge tubes (VWR International LLC, Radnor, PA) with a CF-2 SpectraChrom fraction collector (Spectrum Laboratories Inc., Rancho Dominquez, CA) (Figure 3). The collection time was determined according to the injection velocity and column PV. The vials were weighed before and after collecting the effluent samples to determine the mass collected in each vial.

Once 3.5 PVs of the tracer and 3.5 PVs of the background salt solution were injected into the core, the collected samples were diluted with DI water by a factor of 50 and measured with a bromide probe (Cole-Parmer North America Vernon Hills, IL) in units of mV. The probe measurements are calibrated using a 5-point standard curve, measured at the beginning and end of the bromide measurements, and concentrations of each effluent sample were determined using an exponential equation from the averaged standard measurements. Effluent concentration data for the tracer were modeled using CFITIM3 in STANMOD Version 2.08.1130 to determine the Peclet number (Pe = ...) and retardation factor (R_F=...) and to confirm the pore volume for each column experiment. CFITIM3 is a code used for analyzing observed effluent data using

analytical solutions for one-dimensional equilibrium and non-equilibrium convective-dispersive transport (van Genuchten 1980, van Genuchten and Simunek 1999).

Influent IO NP suspensions were prepared in an Erlenmeyer flask with a magnetic stir bar by adding the concentrated stock IO NP suspension to degassed background salt solution. Prior to injection, the IO NP suspension was adjusted with 1.0 M sodium hydroxide (NaOH) to a pH of 7.0 in order to ensure consistent pH injection for all concentrations of IO NP. Once prepared the magnetic stir bar was removed. Unstable nanoparticle formulations have shown to aggregate and attach onto the magnetic stir bar. The IO NP suspension was then injected at a 12 m/day pore-water velocity (1.00 mL/min injection rate) and collected using the same procedure as the nonreactive tracer described above.

The pressure in the intact core was monitored during Experiments 2, 4, 6, 8, and 9 (Table 2) to observe any permeability changes during NP injection. The Hamilton valve at the bottom of the core was connected to a stainless steel "t" connection that linked to the HPLC pump and to a 100 psi Model AB pressure transducer (Pressure Transducer Data Instruments, Acton, MA). The pressure transducer was connected to a central data acquisition system that recorded the pressure at 20 second intervals. The pressure for each time increment was obtained by subtracting the zero value (voltage value given by pressure transducer when it is open to the atmosphere) from the output voltage, which is then normalized by the input voltage and then multiplied by the pressure transducer calibration factor (351.8 kg*force/cm^2 /v/v). The pressure in kg*force /$cm^2$was then converted to Pa employing the conversion factor, 98,070 N*cm^2/(kg*force*m^2). This pressure was then converted to meters of head. The hydraulic conductivity (*K*) was then calculated using Darcy's law, and later converted to intrinsic permeability (*k*) using the following equation:

$$k = \frac{Q\mu}{A\rho g\frac{dh}{dl}}$$

where Q is the flow rate (m^3/s), μ is the fluid viscosity (kg/ms), A is the cross-sectional area of the column (m^2), ρ is the fluid density (kg/m^3), g is the gravitational constant (m/s^2), dh is the change in head (m), and dl is the column length (m).

3.5 Nanoparticle Characterization and Measurement

The average hydrodynamic diameter and electrophoretic mobility of the nanoparticles was measured at the beginning and end of the experimental injection sequences. These values were obtained using dynamic light scattering (DLS) at 173˚ scattering angle with a Zetasizer Nano ZetaSizer (ZS) Analyzer (Malvern Instruments Ltd., Southborough, MA). Approximately 1.0 mL of IO NP suspension was transferred into a disposable cuvette (Malvern Instruments Ltd.) and analyzed for hydrodynamic size distribution. Prior to use, the ZetaSizer was calibrated using mono-disperse polystyrene spheres (Nanosphere Size Standards, Duke Scientific, Palo Alto, CA) with a mean diameter of 97 ± 3 nm and a zeta potential transfer standard (Malvern Instruments Ltd.) with a mean zeta potential of -68 ± 6.8 mV. Zeta potential measurements were made by transferring the appropriate amount of IO NP suspension into a DTS1070 folded capillary cell (Malvern, Westborough, MA) as indicated on the cell with a syringe needle.

Effluent samples from the core experiments were collected in 15-mL sterile plastic centrifuge tubes (VWR International LLC, Radnor, PA) with a CF-2 SpectraChrom fraction collector (Spectrum Laboratories Inc., Rancho Dominquez, CA). Tracer samples were diluted 50-fold with DI water and measured using a bromide probe (Cole-Parmer North America Vernon

Hills, IL). The probe was calibrated using the equation from a 5-point standard curve measured at the start and end of analysis, and concentrations of each effluent sample were determined using an exponential equation from the averaged standard measurements. The concentration of IO NPs in column effluent samples was determined using ultraviolet-visible (UV) spectroscopy with a Shimadzu UV-1800, 120V instrument (Shimadzu Co rporation, Kyoto, Japan). Absorbance was measured at wavelengths ranging from 400 to 700 nm. A wavelength of 600 nm was used to calibrate and analyze the concentrations of the effluent samples. The calibration wavelength of 600 nm was selected as it was the mid-point of the measured range and the samples had a high R-squared value at this wavelength. A five-point calibration curve was established after each experiment by diluting a stock solution of IO NPs in API brine, adding additional salts to keep the background solution of API brine the same. The effluent IO NP absorbance was plotted against the calibration curve absorbance to determine concentration and was plotted as relative input concentration (C/C_0). The average influent concentration (C_0) was determined from the IO NP injection solution taken at the beginning and end of the NP injection, and C represents the IO NP concentration in each respective effluent sample.

3.6 Solid Phase Concentrations of Magnetite

To determine the distribution of iron retained along the core length, a retention profile was measured. At the completion of each transport experiment, the intact core holder was disassembled, cores were cut into discrete sections (0.8 – 0.5 in.) using a 7” Bridge Tile Saw (Chicago Electric, Carol Stream, IL) equipped with a diamond-tipped saw blade. These sections were then pulverized with a mortar and pestle and dried at approximately 100 °C for at least 24

hours prior to acid digestion.10 mL of trace metal grade $HNO_3$was added to 0.1 g of the pulverized Berea sandstone sectioned pieces. Solid-phase (retained) IO NP was extracted using microwave-assisted digestion with a Discover SP-D, (CEM, Matthews, NC) in concentrated nitric acid (HNO_3). Upon the completion of acid digestion, the supernatant of the digested sample was diluted four-fold in MilliQ water to obtain a background of approximately 4M HNO_3 for ICP-OES analysis. The iron concentration was determined with Optima 5300 Dv (PerkinElmer, Waltham, MA) ICP-OES (inductively coupled plasma optical emission spectrometry). Due to the presence of naturally occurring hematite (the mineral form of iron-oxide), clean cores were analyzed to obtain the background iron content in Berea sandstone.

3.7 Rapid Screening Apparatus

A filter disc apparatus was developed to rapidly evaluate new nanoparticle formulations and the impact of experimental parameters on NP mobility and face plugging behavior. A stainless steel filter containing a Viton O-ring to seal the disc of the tested media (Berea, Bentheimer) was employed. A syringe pump connected to a 1/8" tubing with stainless steel luer-lock connections and 3-way Hamilton valve was utilized to inject the NP solution at 0.5 mL/min in the down-flow direction into the stainless steel filter. The effluent was collected in a prolypropylene Falcon tube (Figure 4). The solid phase used in the filter holder consisted of 2.54 cm (dia.) Berea sandstone or Bentheimer sandstone cores cut into 2 mm thick discs with a diamond-tipped saw blade.

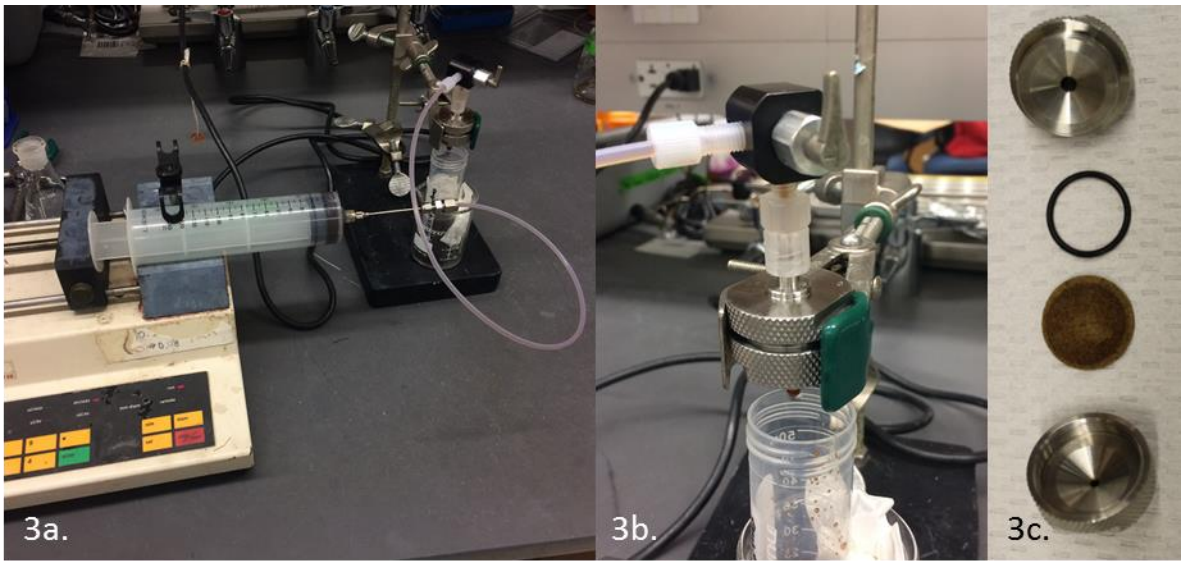

Figure 4. a) Rapid screening apparatus test set-up. A syringe pump connected to a 1/8" tubing with stainless steel luer-lock connections was utilized to inject the NP solution at 0.5 mL/min down-flow into the stainless steel filter. The effluent came out at the bottom of the stainless steel holder connected to a Hamilton valve and 1/8" plastic tubing. b) A close up of the rapid screening apparatus test set-up. c) Stainless steel filter parts, Viton O-ring to seal the disc of the tested media, and 2 mm thick disc of media (Berea, Bentheimer).

Chapter 4: Results

4.1 Straining effects on IO NPs on transport

Physical straining, which can be one of the causes for nanoparticle retention, occurs when the pore throat sizes between grains is not large enough to allow the passage of particles. Straining is considered to be important when d_p/d_{50}, the ratio of particle diameter to the grain diameter at which 50% of the sample's mass is smaller, is greater than 0.0017 or 0.008 (Bradford et al., 2002; Xu et al., 2006). Because d_{50} cannot be determined for consolidated media, the pore throat size to particle size was evaluated instead to determine the presence of straining. The median pore radius of Berea sandstone is 7.41µm (Thomas et al. 2012).

A baseline experiment (Exp #1) was performed to quantify the mobility of the IO NPs in API brine (8% wt. NaCl + 2% wt. $CaCl_2$, ionic strength = 1.9 M) through a Berea sandstone intact core at a pore-water velocity of 12 m/day. In this baseline experiment, a pulse injection (3.6 PVs) of 1000 mg/L of IO NPs in API brine through Berea sandstone resulted in a 45.0% mass breakthrough (Figure 5). With the average hydrodynamic diameter of the IO NP solution particles at approximately 120 nm (Table 3), it is not likely that straining caused the observed retention of NPs. Based on the hydrodynamic diameter distribution curve of the injected IO NP solution and effluent samples of the baseline experiment (Exp #1), which reveals peaks of the influent solution shifted slightly to the right of the peaks of the effluent sample solutions (Figure 6), some of the larger particles were filtered out during the experiment. The average hydrodynamic size of the injection solution was approximately 120 nm while the effluent solution was approximately 95 nm (Table 3). Larger particles in the range of 1000 to 10000 nm were observed in the influent solution that was not seen in the effluent samples (Figure 6),

further indicating the filtering of larger particles. The results of all the intact core experiments conducted are listed in Table 2.

Due to potential variability from one batch of IO NPs to another despite employing the same fabrication process, a second baseline Berea core experiment (Exp #2) was performed for a second batch of IO NPs received. A pulse injection (3.8 PVs) of 1,000 mg/L of IO NPs in API brine through Berea sandstone resulted in a 65.3% mass breakthrough (Figure 5). The average hydrodynamic diameter of both the injection solution and effluent samples was approximately 96 nm (Figure 7, Table 3). The similarity in size between the injection solution and effluent samples indicates that straining did not occur during this experiment.

In addition to the hydrodynamic diameter, zeta potential of the NP injection solution was measured for Experiments 2, 4, 6, 8, and 9 (2nd batch of IO NPs, Table 2). The zeta potential of the NP injection solution ranged from -11.0 mV to -16.2 mV, reflecting moderate stability of IO NP suspension.

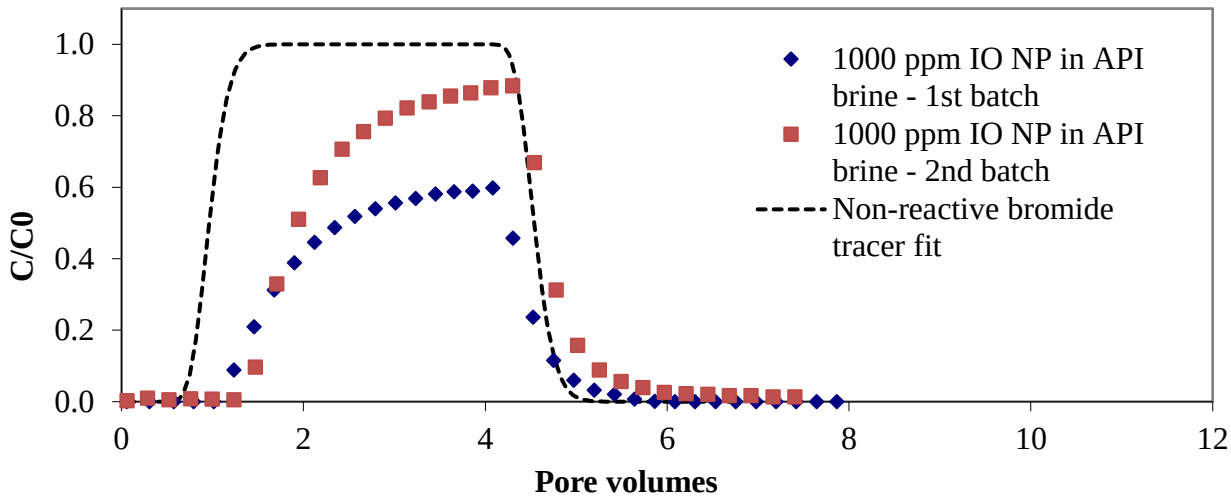

Figure 5. Measured effluent breakthrough curves obtained for pulse injections of 1000 ppm IO NPs in API brine at a nominal pore water velocity of 12 m/day for both batches of IO NPs received (Experiments 1 and 2, Table 2).The dashed line corresponds to a representative nonreactive tracer test.

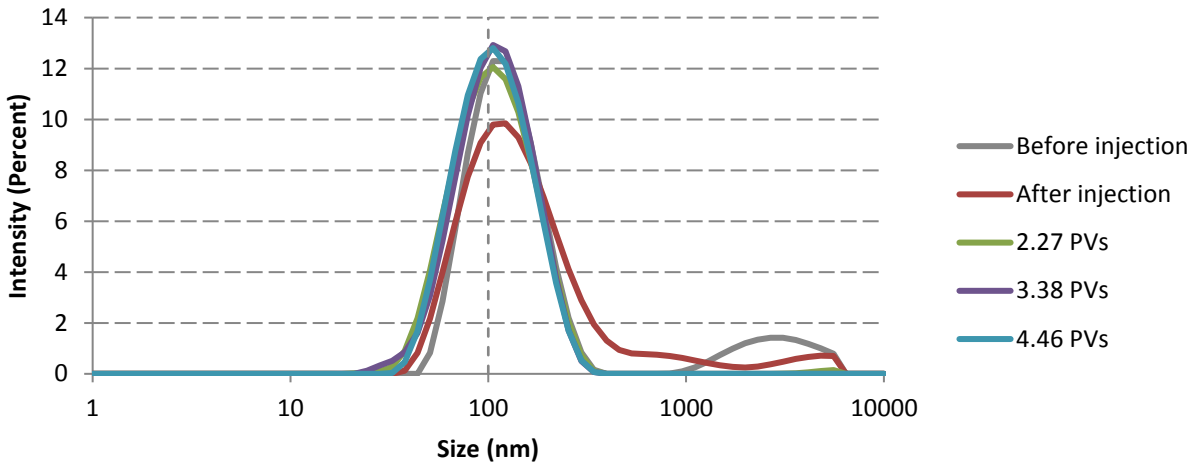

Figure 6. Hydrodynamic diameter distribution curve for 1000 mg/L IO NP injection solution in API brine and effluent samples at different pore volumes as observed in Experiment 1 from batch 1 of IO NPs (Table 2).

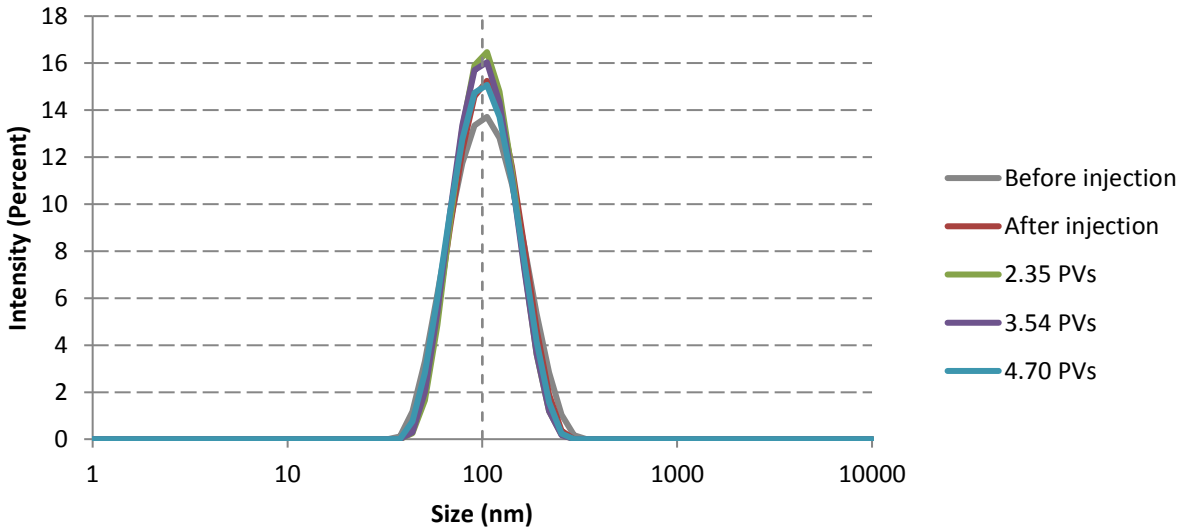

Figure 7. Hydrodynamic diameter distribution curve for 1000 mg/L IO NP injection solution in API brine and effluent samples at different pore volumes as observed in Experiment 2 from batch 2 of IO NPs (Table 3).

Table 2. Summary of intact column experimental conditions and results.

Exp. #	IO NP Conc.[a] (mg/L)	BS[b]	Pulse Width (PVs)	Temp.[c] (˚C)	Polymer	Pe[d]	R_F[e]	IO NP BT[f] (%)	Ret.[g] (µg/g media)	Ret.[h] (mg/ m^2)
1	1000	API brine	3.6	22	N/A	62.39	0.996	45.0	289.0	0.193
2*	1000	API brine	3.8	22	N/A	70.38	1.032	65.3	160.3	0.107
3	1000	0.009 M NaCl	3.7	22	N/A	33.62	1.02	96.0	21.4	0.014
4*	1000	2M NaCl	3.5	22	N/A	86.52	0.971	73.0	125.4	0.084
5	1000	API brine	3.6	22	0.5 PV HEC-10 Preflood (1000 mg/L)	53.33	0.979	63.5	190.8	0.127
6*	1000	API brine	3.3	50	N/A	60.08	1.091	62.6	175.6	0.117
7	100	API brine	33.1	22	N/A	54.07	1.025	63.5	163.0	0.109
8*	100	API brine	13.6	22	N/A	57.76	1.092	17.4	131.2	0.087
9*	250	API brine	14.8	22	N/A	48.71	1.078	59.9	184.6	0.123

All experiments were conducted with Berea sandstone cores at a nominal pore water velocity of 12 m/day.*Experiments conducted with the second batch of nanoparticles. IO NP Conc.[a] = Iron oxide nanoparticle concentrations measured in mg/L as Fe_3O_4. BS[b] = Background solution. Temp.[c] = Temperature at which the experiment was conducted, measured in Celsius. Pec.[d] # = Peclet number, a dimensionless number that represents the ratio of dispersion to advection. RF[e] = Retardation Factor, a dimensionless number that reflects the velocity of particles relative to the background solution (RF of 1 indicates no sorption, particles moving with the background solution). IO NP BT[f] = Iron oxide nanoparticle mass breakthrough measured as a percentage. Ret.[g] = Retention of particles measured as µg/g of media. Ret.[h] = Retention of particles measured as mg/g of media per specific surface area (1.5 m^2/g).

Table 3. Hydrodynamic diameter of IO NP solution influent solution and effluent samples at different pore volumes (PVs shown in parenthesis), measured as nm (Z-average, intensity based). *Experiments conducted with the second batch of nanoparticles.

Experiment	Before Injection	After Injection	Effluent sample 1	Effluent sample 2	Effluent sample 3
1 – 1000 ppm IO NP in API brine	119.4 ± 1.16	120.9 ± 0.70	94.7± 0.05 (2.27 PVs)	95.4± 1.91 (3.38 PVs)	94.3± 1.42 (4.46 PVs)
2* – 1000 ppm IO NP in API brine	96.4 ± 0.82	96.9 ± 1.56	97.3 ± 2.23 (2.35 PVs)	96.1 ± 2.68 (3.54 PVs)	95.4 ± 2.06 (4.70 PVs)
3 – 1000 ppm IO NP in 0.009M NaCl	147.4 ± 0.61	135.0 ± 0.40	126.1 ± 0.57 (2.30 PVs)	129.2 ± 1.32 (3.47 PVs)	126.7 ± 0.70 (4.82 PVs)
4* – 1000 ppm IO NP in 2M NaCl	103.8 ± 2.41	104.7 ± 1.62	102.1 ± 3.13 (2.14 PVs)	102.9 ± 1.66 (3.23 PVs)	102.6 ± 2.14 (4.29 PVs)
5 – 1000 ppm IO NP in API brine, with HEC-10 preflood	116.3 ± 0.32	109.1 ± 0.72	94.4 ± 1.26 (1.56 PVs)	96.5 ± 0.80 (2.68 PVs)	96.6 ± 0.86 (3.79 PVs)
6* – 1000 ppm IO NP in API brine at 50˚C	98.5 ± 0.51	97.0 ± 0.86	98.7 ± 2.21 (2.06 PVs)	98.6 ± 2.10 (3.09 PVs)	97.4 ± 2.04 (4.11 PVs)
7 – 100 ppm IO NP in API brine	93.1 ± 1.15	91.1 ± 2.39	82.3 ± 0.94 (7.25 PVs)	81.5 ± 1.58 (14.91 PVs)	81.6 ± 1.49 (22.47 PVs)
8* – 100 ppm IO NP in API brine	90.5 ± 1.46	91.0 ± 1.78	92.6 ± 1.53 (10.56 PVs)	90.0 ± 1.71 (13.60 PVs)	93.1 ± 1.17 (14.31 PVs)
9* – 250 ppm IO NP in API brine	91.4 ± 1.21	92.1 ± 1.88	91.3 ± 1.20 (6.83 PVs)	90.6 ± 1.09 (11.49 PVs)	90.8 ± 1.38 (14.75 PVs)

Table 4. Zeta potential of IO NP injection solutions measured in mV obtained using DTS1070 folded capillary cell with a Zetasizer Nano ZS Analyzer. *Experiments conducted with the second batch of nanoparticles.

Experiment	Zeta Potential (mV)
2* – 1000 ppm IO NP in API brine	-13.8 ± 3.13
4* – 1000 ppm IO NP in 2M NaCl	-16.2 ± 2.27
6* – 1000 ppm IO NP in API brine at 50˚C	-11.0 ± 1.54
8* – 100 ppm IO NP in API brine	-11.5 ± 2.98
9* – 250 ppm IO NP in API brine	-13.2 ± 4.32

4.2 Effects of Salinity and Polymers on IO NP transport

Three additional intact core flood experiments were conducted to evaluate the impact of salinity and a polymer preflood on IO NP transport through intact Berea sandstone cores. With a background solution of API brine (Exp #1), 45% mass breakthrough of the injected IO NPs was observed, while a background solution of 500 mg/L NaCl (ionic strength = 0.009 M) resulted in a significantly higher mass breakthrough of 96% (Exp #3, Figure 8, Table 2). An additional column experiments (Exp #4) was conducted with a background solution of 2 M NaCl (same ionic strength as API brine) to evaluate the impact of monovalent versus divalent cations. A pulse injection (3.5 PVs) of 1,000 mg/L of IO NPs in 2M NaCl through Berea sandstone resulted in a 73.0% mass breakthrough (Figure 9, Exp #4) compared to the 65.3% mass breakthrough with an API brine background solution (Exp #2).

According to the DLVO theory, the sum of the Van der Waals attractive forces and the repulsive forces from the electrostatic double layer determines the attachment behavior of particles (Hotze et al., 2010). In the presence of divalent cations, there is a strong suppression of the electrical double layer and Van der Waals forces dominate, which lead to aggregation (Wang et al., 2008). In Exp #4, which evaluated the mobility of IO NPs in the absence of divalent

cations but at the same ionic strength as API brine, removing divalent cations only improved the mobility of IO NPs by approximately 12% with a mass breakthrough of 73.0%. This result suggests for the NPs studied in this work, the presence of divalent cations had a minimal impact on the electrical double layer suppression, resulting in slight improvement in IO NP mobility. Furthermore, the slight improvement in IO NP mobility in the absence of divalent cations in Exp #4 reveals that the bridging complexation, in which the Ca^{2+} serves as a bridge between the cation-exchange locations (Torkzaban et al., 2012) on the negatively charged clay surface and the negatively charged poly(AMPS-co-AA) group on the IO NPs, is not a major contributor to the retention mechanism of these IO NPs. Based on the results of Exp. #4 (Table 2), the greatly improved recovery of IO NPs seen with background solution of 0.009M NaCl (Exp #3) was attributed to the substantially reduced ionic strength, rather than the absence of divalent cations (i.e., cation bridging). At low ionic strengths the electrical double layer extends far out from the particle, resulting in repulsion forces that inhibit attachment (Hotze et al., 2010). In contrast to the results of this current study, Xue et al. (2014) observed 40% more retention of NPs on 40-50 mesh Ottawa sand (d_{50} = 354 μm) with a background solution containing divalent cations (Ca^{2+}) compared to a background solution containing only monovalent salt (NaCl) at an equivalent ionic strength (1.9 M). These contrasting findings indicate the particles utilized in the experiments for this current study, which were synthesized in triethylene glycol unlike the particles employed in study of Xue et al. (2014), are more affected by ionic strength than the presence of divalent cations. The slower flow rate (pore-water velocity of 2.9 m/day, compared to the 12 m/day used in this study) employed for their column studies (Xue et al., 2014) is also a potential source of the contrasting findings.

A polymer preflood of 0.5 PVs of hydroxyethyl cellulose (HEC-10) in API brine increased the breakthrough of IO NPs by 41% compared to when no polymer was utilized (corresponding to a 63.5 % mass breakthrough) (Exp # 5, Figure 8, Table 2). The increased breakthrough of IO NPs from the polymer preflood is consistent with the findings of Kmetz et al. (2016), in which IO NP recovery from crushed Berea sandstone improved by 20% with a HEC-10 preflood. These results suggest that HEC-10 screens the IO NP attachment sites in both unconsolidated and consolidated media.

After experiments were run, the intact Berea sandstone cores were visually inspected and reddish-brown discoloration on the inlet face was observed for the experiment run with an API brine background (Exp. # 1, 2, 4, 6, 7, 8, and 9, Table 2), which was attributed to the retention of IO NPs (Figure 10 and 11, Table 5 and 6). In contrast, the outlet face shows no color change compared to the core before nanoparticle injection. The visible retention of IO NPs was mitigated with a HEC-10 preflood and when the background solution was 500 mg/L (0.009 M) NaCl (Figure 10). However, this face caking of IO NPs was not reduced with 2M NaCl as the background solution (Figure 11), further supporting the strong influence of ionic strength on IO NP mobility. The solid retention analysis of the cores reveal more retention of Fe_3O_4 at the inlet face than the outlet face for the experiments conducted with 1,000 mg/L of IO NP in API brine for both batch 1 and 2 (Table 5 and 6), supporting that the dark staining of the inlet face can be attributed to the retention of the IO NPs. However, in the other experiments where staining of the inlet face occurred (Experiments 3, 4, 6, 7, 8, and 9, Table 2), the solid retention analysis failed to show more retention of Fe_3O_4 at the inlet face than the outlet face (Table 5 and 6). This discrepancy can be attributed to the large natural iron content of the Berea core. As a result,

when a significant amount of retention is not occurring, it is difficult to detect the retained Fe_3O_4 in a media with a high Fe background content (7.36 ± 0.493 mg Fe_3O_4/g of media).

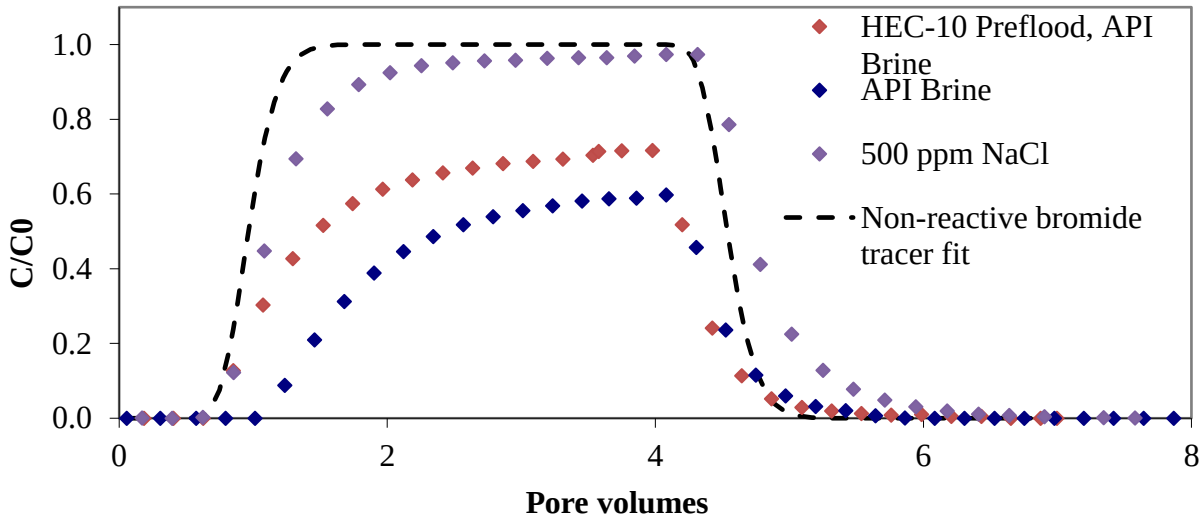

Figure 8. Measured effluent breakthrough curves obtained for pulse injections of 1000 ppm IO NPs with background solutions of API brine, API brine and 0.5 PV of HEC-10 preflood, or 500 ppm NaCl in intact Berea sandstone core at a nominal pore water velocity of 12 m/day (Experiments 1, 3, and 5, Table 2). The dashed line corresponds to a representative nonreactive tracer test.

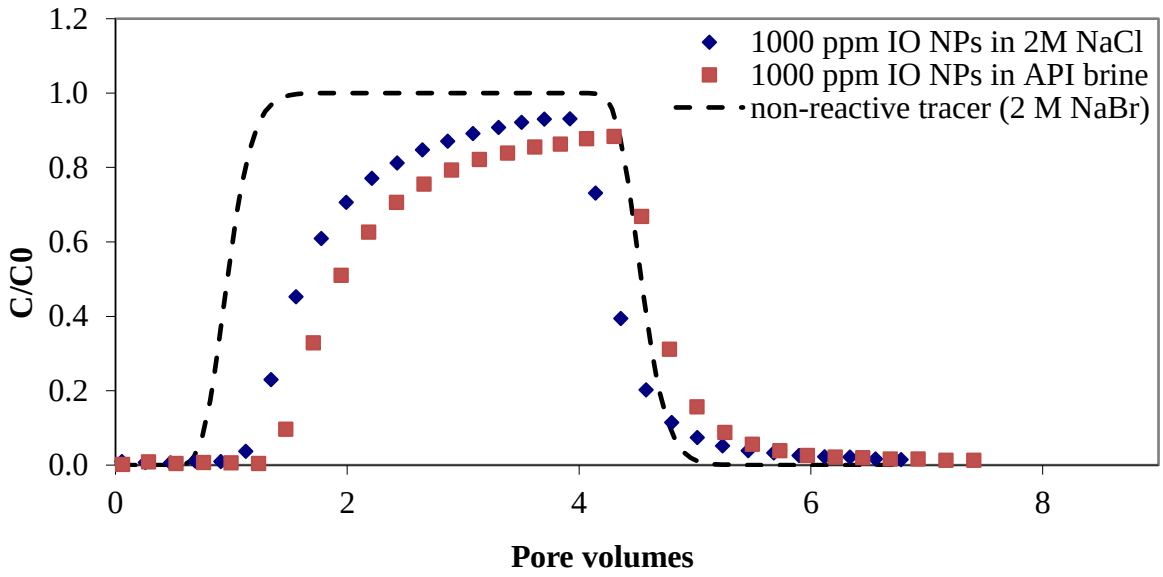

Figure 9. Measured effluent breakthrough curves obtained for pulse injections of 1000 ppm IO NPs with background solution of API brine and 2 M NaCl in intact Berea sandstone core at a nominal pore water velocity of 12 m/day (Experiments 2* and 4*). The dashed line corresponds to a representative nonreactive tracer test. *Experiments conducted with the second batch of nanoparticles.

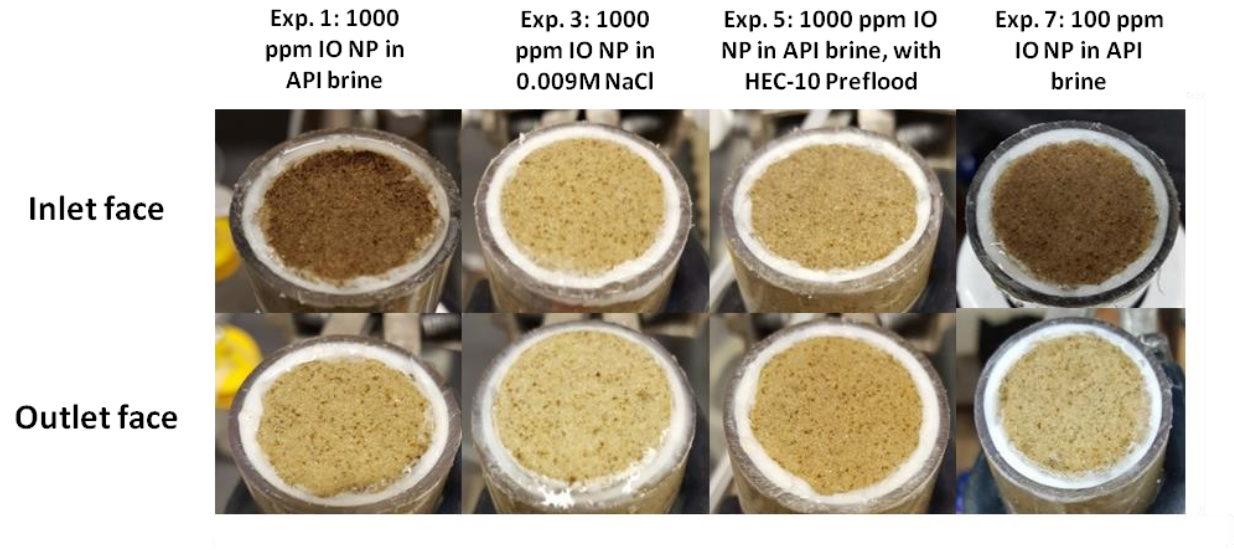

Figure 10. Inlet and outlet faces of the intact Berea sandstone cores after each respective experiment with batch 1 of IO NPs was performed: 1000 mg/L IO NP in API brine, in API brine with 0.5 PVs of HEC-10 preflood,in 500 mg/L NaCl, and 100 mg/L IO NP in API brine.

Table 5. Inlet and outlet retention values (mg Fe_3O_4/g of media) for intact Berea sandstone cores after each respective experiments with batch 1 of IO NPs was performed: 1000 mg/L IO NP in API brine, in API brine with 0.5 PVs of HEC-10 preflood, in 500 mg/L NaCl, and 100 mg/L IO NP in API brine.

	Exp. 1: 1000 ppm IO NP in API brine	Exp. 3: 1000 ppm IO NP in 0.009M NaCl	Exp. 5: 1000 ppm IO NP in API brine with HEC-10 Preflood	Exp. 7: 100 IO NP in API brine
Inlet Face Retention (mg Fe_3O_4/g of media)	1.98	1.33	1.01	0.74
Outlet Face Retention (mg Fe_3O_4/g of media)	1.49	1.16	1.04	0.84

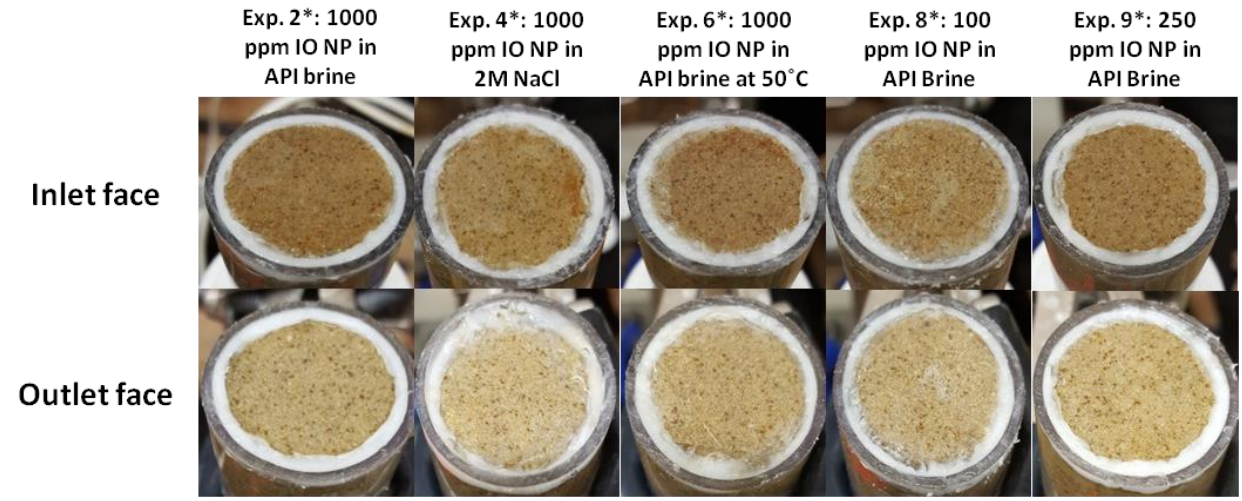

Figure 11. Inlet and outlet faces of the intact Berea sandstone cores after each respective experiment with batch 2 of IO NPs was performed: 1000 mg/L IO NP in API brine, in API brine at 50ºC, in 2M NaCl, 100 mg/L IO NP in API brine, and 250 mg/L IO NP in API brine. *Experiments conducted with the second batch of nanoparticles.

Table 6. Inlet and outlet retention values (mg Fe_3O_4/g of media) for intact Berea sandstone cores after each respective experiments with batch 2 of IO NPs was performed: 1000 mg/L IO NP in API brine, in API brine at 50ºC, in 2M NaCl, 100 mg/L IO NP in API brine, and 250 mg/L IO NP in API brine. *Experiments conducted with the second batch of nanoparticles.

	Exp. 2*: 1000 ppm IO NP in API brine	Exp. 4*: 1000 ppm IO NP in 2M NaCl	Exp. 6*: 1000 ppm IO NP in API brine at 50ºC	Exp. 8*: 100 ppm IO NP in API brine	Exp. 9*: 250 ppm IO NP in API brine
Inlet Face Retention (mg Fe_3O_4/g of media)	1.56	0.62	0	1.20	0.53
Outlet Face Retention (mg Fe_3O_4/g of media)	0.39	2.05	0.95	1.74	0

4.3 Temperature Effects on IO NP transport

The effect of temperature on IO NP mobility in Berea sandstone was investigated by conducting transport experiments at 50ºC. A pulse injection (3.3 PVs) of 1000 mg/L of IO NPs in API brine through Berea sandstone conducted at 50ºC resulted in a 62.6% mass breakthrough compared to the 65.3% mass breakthrough when the experiment was conducted at room temperature (22ºC) (Exp #2 Figure 12). The similar mass breakthrough observed at the two temperatures (22 and 50 ºC) reveal the high stability of these IO NPs. Several transport studies have reported increased retention at higher temperatures due to the reduced energy barrier for adsorption (Ghatbandhe et al., 2013; Sasidharan et al., 2016). Ghatbandhe et al. (2013) observed increasing uptake capacity of activated carbon for 2, 4-Dichlorophenoxyacetic Acid with increasing temperature from 25ºC to 45ºC. Sasidharan et al. (2017) observed an increase up to 109% in attachment rate coefficient (k_{att})of carboxyl-modified latex nanoparticles on ultra-pure quartz sand (125 – 300 nm) and an increase up to 160% in the percentage of the sand surface area that contributed to attachment (S_f) when the temperature was increased from 4 to 20ºC at ionic strengths of 10 and 30 mM. Conversely, this same temperature range had negligible effect on k_{att} and S_f values when the ionic strength was greater than 50 mM due to the elimination of the energy barrier at low zeta potentials of the sand and particles (Sasidharan et al., 2017). The results from the present study show that with a background solution of API brine (2M ionic strength) increasing the temperature did not affect the mobility of IO NPs, consistent with the findings of Sasidharan et al. (2017). These findings are very encouraging, and suggest that in standard reservoir conditions of high salinity, temperature will not affect the transport of these IO NPs.

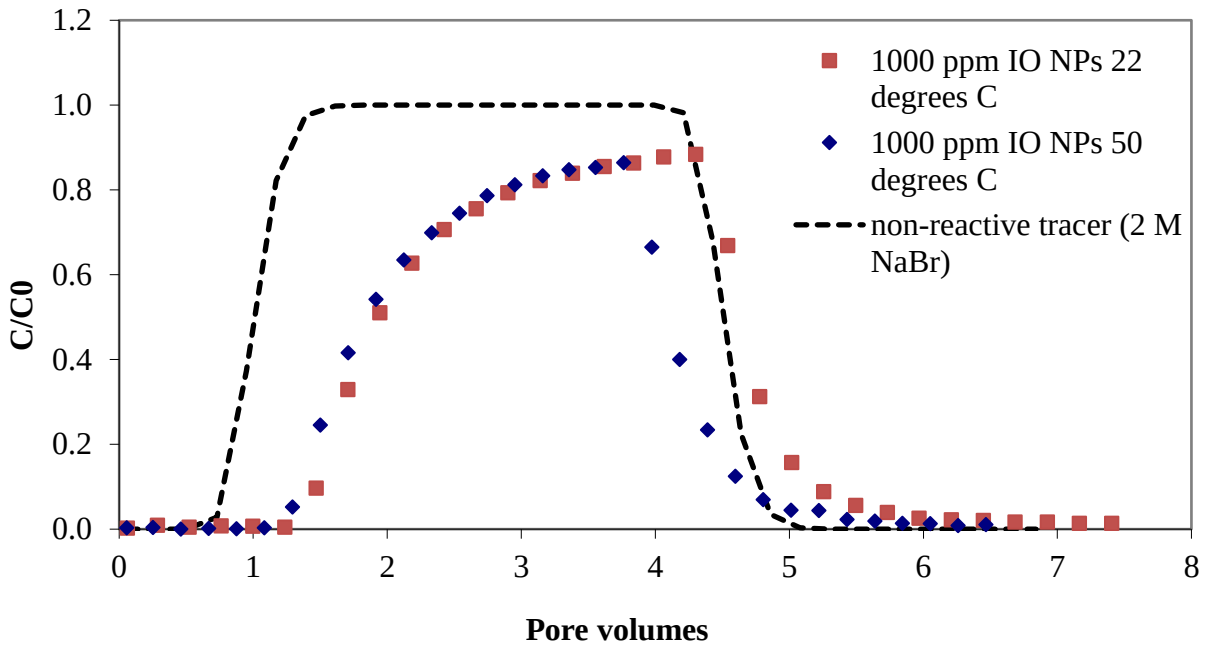

Figure 12. Measured effluent breakthrough curves obtained for pulse injections of 1000 ppm IO NPs with background solution of API brine at 22˚C and 50˚Cin intact Berea sandstone core at a nominal pore water velocity of 12 m/day (Exps. # 2* and 6*). The dashed line corresponds to a representative nonreactive tracer test. *Experiments conducted with the second batch of nanoparticles.

4.4 Effects of Iron Oxide Nanoparticle Concentration on Transport

In addition to the effects of salinity and polymer use, the effect of IO NP concentration was also evaluated. To evaluate the effect of concentration, 100 mg/L of IO NPs with background solution of API brine was injected for 33 PVs (~10x the PVs injected for 1000 mg/L of IO NPs in API brine). Injecting the same amount of mass at a lower concentration of 100 mg/L IO NPs in API brine through Berea sandstone resulted in a mass breakthrough of 63.5% compared to the 45.0% breakthrough at 1000 mg/L (Exp # 7, Figure 13). While the 1000 mg/L injection had a breakthough (pore volume at which the IO NP can be measured in the effluent) at

around 1.5 PV, the 100 mg/L injection had a breakthrough at approximately 3 PVs. A replicate experiment was conducted using the second batch of IO NPs to see if the delayed breakthrough could be reproduced. At 1,000 mg/L, a 3.8 PV injection in API brine through Berea sandstone resulted in a breakthrough at 1.5 PVs and a mass recovery of 65.3% (Exp #2, Figure 14). At 100 mg/L, a 13.6 PV injection in API brine resulted in a significantly delayed breakthrough at approximately 8.5 PVs and a mass recovery of 17.4% (Exp #8, Figure 14). The longer delayed breakthrough observed for the second batch of IO NPs at 100 mg/L may be a result of variability in particle fabrication technique or coating technique used from one person to another since each batch was prepared by someone different. At 250 mg/L, a 14.8 PV (same mass as 1000 mg/L injection in Exp# 9) injection in API brine resulted in a delayed breakthrough at approximately 3 PVs and a mass recovery of 59.9%,similar to the mass recovery at 1000 mg/L (65.3% mass breakthrough, Exp #2) (Figure 14).

A similar breakthrough mass when the same amount of mass is injected (Exps. 1 and 7; Exps. 2 and 9, Table 2) is consistent with a limiting or maximum retention capacity, which has been reported for other nanoparticles including nanoscale fullerene aggregates (nC_{60}). As demonstrated by Li et al., (2008), larger initial injection concentration results in rapid saturation of the particle deposition sites, which results in a faster mass recovery in the column effluent. Therefore, decreasing IO NP injection concentration results in a delayed breakthrough due to the reduced number of IO NPs there are to screen the available attachment sites. Furthermore, by injecting the same amount of mass, even at lower concentrations, the same number of deposition sites is occupied resulting in similar mass recoveries. According to Li et al. (2008), the transport of nanoscale fullerene aggregates (nC_{60}) through water-saturated porous media can be described using a one-dimensional mathematical model that utilizes the effective attachment rate ($k_{att}\psi$).

While k_{att} is the attachment rate, the site blocking function (ψ) can be described as a function of S_{max}, a value that represents the maximum attainable particle concentration on the sand surface:

$$\psi = 1 - S/S_{max}$$

where S is the attachment at the specific time. The value of ψ decreases as more nC_{60} aggregates are deposited on the grain surface, resulting in a reduction of $k_{att}\psi$, where $k_{att}\psi$ approaches a value of 0 as S approaches S_{max} (Li et al., 2008). In experiments 1 and 7 and experiments 2 and 9, with the same amount of mass injected in the two sets of experiments, S has reached the maximum attachment capacity, resulting in similar breakthrough masses. In experiment 8 at 100 mg/L IO NP injection, because less mass has been injected than the mass injected in Exp #2, S has yet to reach S_{max}, and the IO NPs continues to be attached to the mineral surface of the Berea sandstone resulting in a significantly delayed breakthrough (8.5 PVs) and a low mass recovery of 17.4%. It is important to note that with crushed Berea sandstone (CBS), crushing the material makes more fines available, increasing the surface area of the available grains and therefore increasing the S_{max}. As a result, despite having the same mineral composition as an intact Berea sandstone, CBS will have a higher attachment capacity, and transport behaviors in CBS will not accurately depict transport behaviors in intact Berea sandstone, highlighting the importance of conducting experiments in consolidated media.

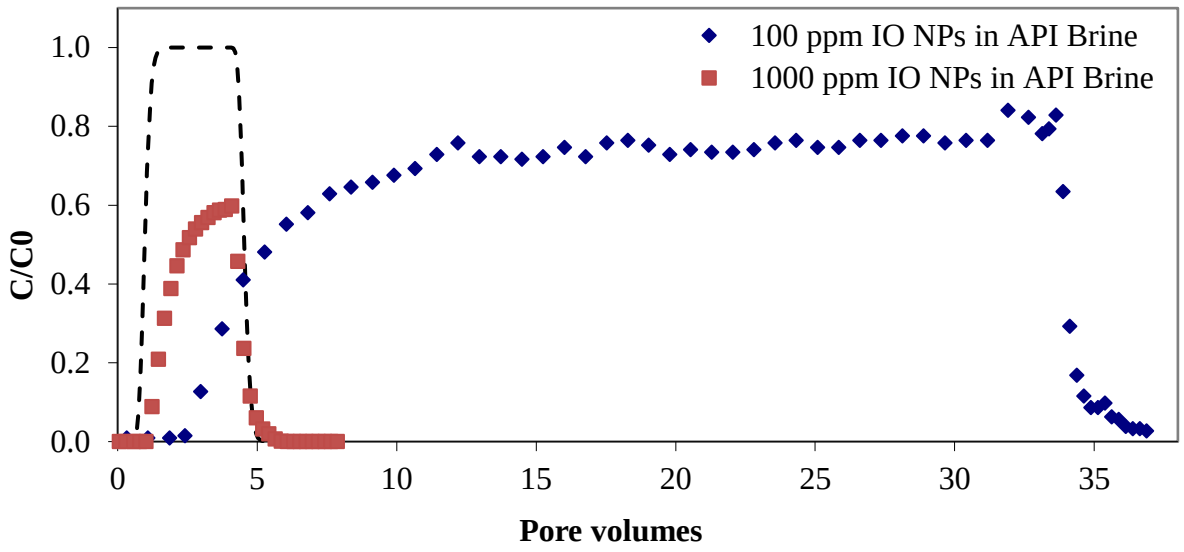

Figure 13. Measured effluent breakthrough curve for 3.6 PV injection of 1000 ppm IO NPs and 33.1 PV injection of 100 mg/L IO NPs both with background solution of API Brine in intact Berea sandstone core at a nominal pore water velocity of 12 m/day (Exps. 1 and 7). The dashed line corresponds to a representative nonreactive tracer test. Both experiments were conducted with the first batch of IO NP solutions.

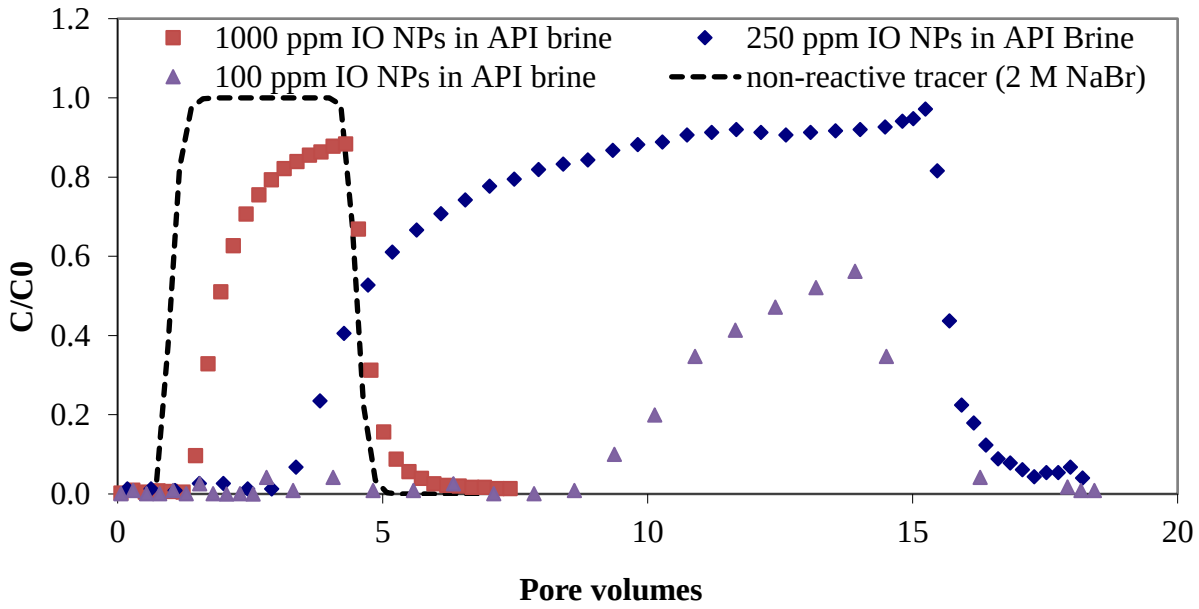

Figure 14. Measured effluent breakthrough curve for 3.8 PV injection of 1000 ppm IO NPs, 13.6 PV injection of 100 mg/L IO NPs, and 14.8 PV injection of 250 mg/L IO NPs all with background solution of API Brine in intact Berea sandstone core at a nominal pore water velocity of 12 m/day (Exps. 2*, 8*, and 9*). The dashed line corresponds to a representative nonreactive tracer test. *Experiments conducted with the second batch of nanoparticles.

4.5 Solid Phase Retention of IO NPs

The solid phase (retained) IO NPs retention profile was obtained using microwave-assisted acid digestion and analysis for iron by ICP-OES, as described in the experimental methods section (Figures 15 and 16). Due to the high background content of iron oxide in Berea sandstone (7.36 ± 0.493 mg Fe_3O_4/g of media) compared to the retained iron from the NP injection, it was difficult to detect the retained Fe_3O_4. Thus, a reliable retention trend over the length of the core was unable to be obtained. In Exp #1, where retained IO NP particles was visually observed at the inlet face of the core after the experiment (Figure 10), a hyperexponential retention profile, which is often indicative of physical straining (Li et al., 2008), was not observed. Instead, the solid retention profile reveals slightly more retention at the inlet face and consistent retention in the rest of the core's length (Figure 15). In Exp #4, while retained IO NP was also observed at the inlet face compared to the clean outlet face of the core (Figure 11), the solid retention profile for Exp #4 reveals an erratic retention profile with more IO observed at the outlet of the core than the inlet of the core (Figure 16). This contrasting finding from the visual inspection of the core faces and no observable trends in the solid retention profile (Figure 16) reveals solid retention analysis as an unreliable means of determining real IO retention trends along the core in the presence of a high background iron content. The error bar (± 0.493 mg Fe_3O_4/g of media) shown in the solid retention figures (Figure 15 and 16) was determined by measuring standard deviation of the iron content in blank Berea sandstone cores.

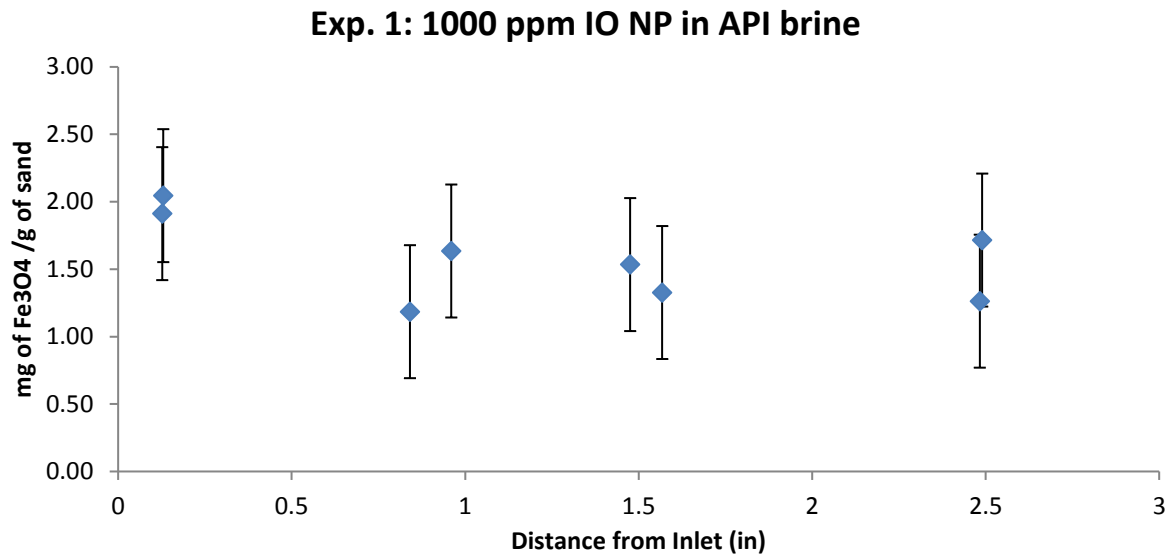

Figure 15. Solid retention profile for 3.6 PV injection of 1000 mg/L IO NP in API brine (Experiment 1, Table 2).

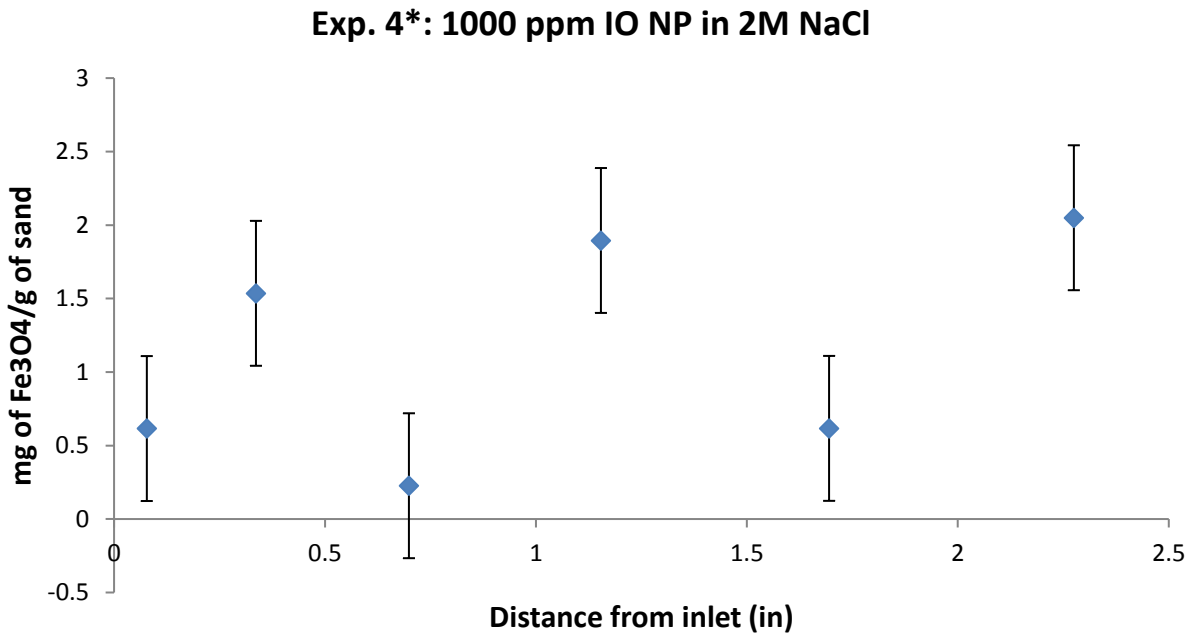

Figure 16. Solid retention profile for 3.5 PV injection of 1000 mg/L IO NP in 2M NaCl (Experiment 4*, Table 2). *Experiments conducted with the second batch of nanoparticles.

4.6 Additional measurements

The pressure in the intact core was monitored for Experiments 2, 4, 6, 8, and 9 (second batch of NP solution - Table 2) to observe any permeability changes during NP injection. Permeability values remained constant during the NP injection of experiments conducted with the second batch of NP solutions. The permeability remained constant around 0.22 Darcy during the 3.8 PV injection of 1000 mg/L IO NP in API brine (Figure 17, Exp 2, Table 2). The permeability values lie in the range of the reported values, 198 to 249 mD with an average of 223 mD and standard deviation of 20.41 (Thomas et al. 2012).

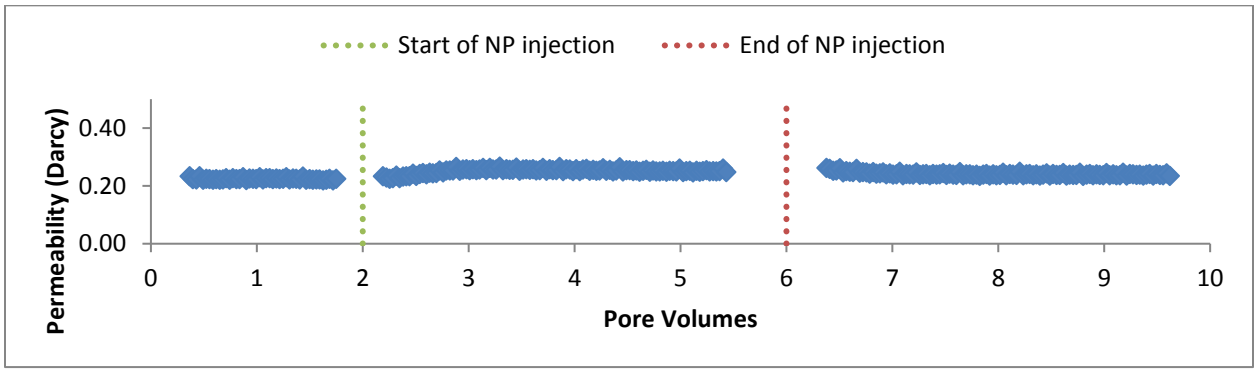

Figure 17. The permeability of the Berea sandstone core measured with a pressure transducer during the 3.8 PV injection of 1000 mg/L IO NP in API brine (experiment 2*, Table 2). The permeability remains constant around 0.22 Darcy during the NP injection. *Experiments conducted with the second batch of nanoparticles.

4.7Rapid Screening Apparatus

A filter disc apparatus was developed to rapidly evaluate new nanoparticle formulations and the impact of experimental parameters on NP mobility and face plugging behavior. When 30 mL of 1,000 mg/L IO NP in API brine was injected at 0.5 mL/min, retention of IO NPs, shown

as reddish-brown discoloration, was visualized on both Berea and Bentheimer discs (Figure 18). The visible retention of IO NPs was mitigated for both medias when the injection solution was prepared in deionized (DI) water, (Figure 18). Retention analysis, using the same method elaborated in section 3.6, of the discs reveals much higher retention of IO NPs under API brine (1.206 mg Fe_3O_4/g media for the Berea and 0.089 mg Fe_3O_4/g media in Bentheimer) than in DI water (0.344 mg Fe_3O_4/g media in Berea and 0.002 mg Fe_3O_4/g media in Bentheimer) (Table 7). The background iron content of clean media (6.698 mg Fe_3O_4/g media in Berea and 0.084 mg Fe_3O_4/g media in Bentheimer) was analyzed and corrected for in the retention analysis. This rapid screening apparatus was able to replicate the retention behavior seen on the inlet face from intact core experiments at different ionic strengths of the background solution. The influent and effluent hydrodynamic size shows little change during the rapid screening test consistent with the behavior of the second batch of IO NPs used in experiments 2, 4, 6, 8 and 9 (Table 8).

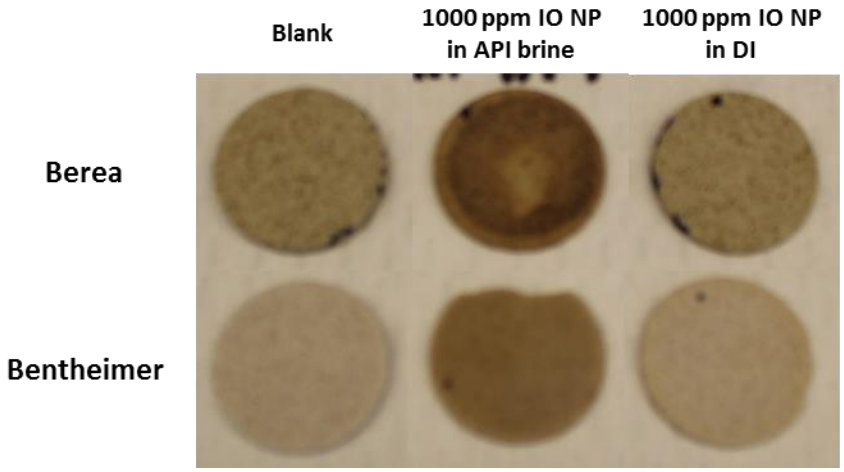

Figure 18. Inlet faces of the Berea and Bentheimer discs after the rapid screening test, in which 30 mL of 1000 mg/L IO NP in API brine or DI water was injected at 0.5 mL/min.

Table 7. Retention analysis (percent retained shown in parenthesis) of IO NPs in the Berea and Bentheimer discs used for the rapid screening test.

Media	**1000 ppm IO NP in API brine**	**1000 ppm IO NP in DI**
Berea	1.206 mg Fe_3O_4/g media (1.66%)	0.344 mg Fe_3O_4/g media (0.42%)
Bentheimer	0.089 mg Fe_3O_4/g media (0.15%)	0.002 mg Fe_3O_4/g media (0%)

Table 8. The hydrodynamic diameter of IO NP solution influent and effluent during the rapid screening experiment.

	Size (nm) ± std. dev			
	Berea		Bentheimer	
Sample	influent	effluent	influent	effluent
1000 mg/L IO NP in API brine	148±1.9	158±1.1	164±2.2	160±2.4
1000 mg/L IO NP in MilliQ	148±1.3	150±2.4	149±1.6	149±3.6

Chapter 5: Conclusion

There have been very few nanoparticle mobility studies conducted using intact sandstone cores (Yu et al., 2014 and Mohammed et al., 2012). With 22 out of 32 billion barrels of oil produced coming from sandstone reservoirs (Sheng 2011), it is important to extend our understanding of NP transport behavior from unconsolidated media to intact consolidated cores. In prior studies, surface-treated IO NPs were observed to be successfully transported through Boise sandstone (750-1000 mD) (> 95% breakthrough) at low salinity (3% wt. NaCl) (Yu et al., 2014), and individual effects of NP size, shape, and surface charge on NP transport in Berea sandstone has been observed (Mohammed et al., 2012).This thesis evaluated other parameters including elevated temperature, concentration, pre-filtration, salinity, and polymer-use. Key contributions of this work are:

1. The application of the DLVO theory to consolidated media and the finding of ionic strength as a more influential contributor to the electrical double layer than the presence of divalent cations. The experiments conducted at varying input concentrations validated the concept of the limiting or maximum retention capacity, where once the attachment sites are saturated similar mass breakthroughs should be observed. Slight straining was observed in the first batch of IO NPs, but the second batch showed no straining demonstrated by the lack of change in the hydrodynamic size measurements of the influent and effluent IO NP suspensions and the non-hyperexponential profile observed in the solid retention profile.
2. Incorporating a HEC-10 preflood improved the mass recovery by 41%, indicating that the site blocking mechanism of polymers is applicable to both unconsolidated and consolidated media tested.

3. The mobility of IO NP was not affected by temperature, demonstrating the high stability of the IO NPs under the new NP formulation, which involves synthesis of the particles in triethylene glycol (TEG).
4. A rapid screening test was developed to successfully reproduce the inlet face retention behavior observed from intact core experiments under varying ionic strength solutions.

These experiments were used to understand the factors that influence nanoparticle transport in consolidated media so that successful technologies in the field can be designed and implemented. The new batch of IO NPs shows improved mobility, which is a crucial requirement for successful implementation in the field. The results from this study suggests that elevated temperatures observed in high salinity subsurface reservoir conditions will have negligible effect on the transport behaviors of these IO NPs. While electrolyte species will affect the mobility of these IO NPs, variables such as ionic strength of the reservoir fluid will have a much greater influence on its transport behavior. As mobility of these IO NPs will be more affected in some reservoirs (high ionic strength) than others, it is important to understand the geochemistry of the reservoir. Furthermore, if low enough retention cannot be obtained for stable particles in the field, a sacrificial polymer such as HEC-10 can be employed as a site-blocking agent. Once the attachment sites in the reservoir media is saturated, low concentrations of NP injection fluid can be injected, which will exhibit similar recoveries as high concentration NP injection solutions. By employing a polymer preflood and injecting a lower concentration of IO NPs, we can significantly reduce the amount of NPs required for a field study, which is an important economic consideration.

While further developments need to be made with the rapid screening apparatus, the successful simulation of face caking behavior observed at different salinity conditions reveal the potential to use this screening tool as a means to rapidly evaluate the mobility of new nanoparticle formulations. Employing this rapid screening apparatus will allow one to eliminate the need to run column tests on NP formulations that perform poorly. Additionally, utilizing a thin disc as the porous media in this rapid screening apparatus allows one to inject many pore volumes, revealing the capacity at which the media will be plugged up. This information can be used to determine the maximum amount of NP solution that could be injected in a reservoir.

Future work includes employing the experimental parameters from the independent studies of salinity, input concentration, pre-filtering as well as polymer use and temperature to model variety of reservoir conditions. These experimentally validated models will be key to analyzing the subsurface formation when observing the movement of the superparamagnetic IO NPs in the field. Experiments testing similar parameters can be conducted in 2-dimensional and 3-dimensional scales to see if the IO NPs will exhibit similar behaviors in recovery and breakthrough times. These tests will also allow one to see if the models developed from the one-dimensional column studies can be translated to 2 dimensional and 3 dimensional tests. Column studies in other media such as Bentheimer will allow us to evaluate IO NP transport behavior in media of different mineral compositions. Furthermore, media such as Bentheimer, which has a low natural iron content (0.084 mg Fe_3O_4/g media), can be used to extract solid retention profiles of the retained IO NPs. While conducting experiments with intact core plugs allowed us to evaluate IO NP transport behavior in similar media commonly found in potential oil reservoirs, conducting column tests in commercial core holders will allow us to evaluate IO NP mobility at elevated pressures and temperatures that more closely resemble existing oil reservoirs.

Additionally, while this study focused on IO NPs as contrast agents for subsurface oilfield reservoirs, the findings could be relevant for other types of NPs and other applications, such as imaging of salt-water impacted aquifers or in cases where iron NPs are used for environmental remediation.

References

Alexiou, C., et al. (2003). "Magnetic drug targeting – biodistribution of the magnetic carrier and the chemotherapeutic agent mitoxantrone after locoregional cancer treatment. Journal of Drug Target**11**(3): 139-149.

Bean, C. P. and J. D. Livingston (1959). "Superparamagnetism." Journal of Applied Physics**30**(4): 120S-129S.

Bradford, S.A., et al. (2002). "Physical factors affecting the transport and fate of colloids in saturated porous media." Water Resources Research**38**(12): 63-1-63-12.

Chertok, B., et al. (2008). "Iron oxide nanoparticles as a drug delivery vehicle for MRI monitored magnetic targeting of brain tumors." Biomaterials**29**: 487-496.

Cormode, D.P., et al. (2008). "Nanotechnology in Medical Imaging: Probe Design and Applications." Journal of the American Heart Association**29**: 992-1000.

E.I.A. (2013). International Energy Outlook 2013. U. D. O. Energy. Washington D.C., Energy Information Administration: 312.

Espinosa, D., et al. (2010). SPE 129925: "Nanoparticle-stabilized CO_2 foams for potential mobility control applications."Society of Petroleum Engineers.

ExxonMobil (2017). The Outlook for Energy: A View to 2040. Irving, Texas,USA: 76.

Ghatbandhe, A.S. et al. (2013). "Evaluation of Thermodynamic Parameters of 2, 4-Dichlorophenoxyacetic Acid (2, 4-D) Adsorption." Journal of Chemistry ID 519304.

Hong, Y., et al. (2009). "Transport of iron-based nanoparticles: Role of magnetic properties." Environmental Science & Technology**43**(23): 8834-8839.

Hotze, E.M. et al. (2010). "Nanoparticle Aggregation: Challenges to Understanding Transport and Reactivity in the Environment." Journal of Environmental Quality**39**(6): 1909-24.

Kmetz, A.A. et al. (2016). "Improved Mobility of Magnetite Nanoparticles at High Salinity with Polymers and Surfactants." Energy&Fuels**30**(3): 1915-1926.

Li et al. (2008). "Investigation of the Transport and Deposition of Fullerene (C60) Nanoparticles in Quartz Sands under Varying Flow Conditions." Journal of Environment Science and Technology**42**: 7174-7180.

Ludwig et al. (2005). "Oxide Nanoparticle Uptake in Human Lung Fibroblasts: Effects of Particle Size, Agglomeration, and Diffusion at Low Concentrations." Environmental Science & Technology**39**(23): 9370-9376.

Matteo, C., et al. (2012). "Current and Future Nanotech Applications in the Oil Industry." American Journal of Applied Sciences**9**(6):784-793.

Maximova, N. and Dahl O., (2006). "Environmental Implications of Aggregation Phenomena: Current Understanding." Current Opinion in Colloid & Interface Science**11**: 246-266.

Mohammed, A. et al. (2010). "In-situ Multifunction Nanosensors for Fractured Reservoir Characterization." Stanford University. Thirty-Fifth Workshop on Geothermal Reservoir Engineering.

Moridis et al. (2001). "Process for Guidance, Containment, Treatment, and Imaging in a Subsurface Environment Utilizing Ferro-fluids." United States Patent.

Muhammad, I., et al. (2016). Paper in progress

Prabha, S. et al. (2002). "Size dependency of nanoparticle-mediated gene transfection: Studies with fractionated nanoparticles." International Journal of Pharmaceutics**244**(1-2): 105-115.

Prodanovic, M., et al. (2010). SPE 129850: Effects of Magnetic Field on the Motion of Multiphase Fluids Containing Paramagnetic Particles in Porous Media. SPE/DOE Symposium on Improved Oil Recovery. Tulsa, OK, Society of Petroleum Engineers. **2**: 893-911.

Pulfer, S.K., et al. (1999). "Distribution of small magnetic particles in brain tumor-bearing rats." Journal of Neurooncology**41**: 99-105.

Raj, K. and R. Moskowitz (1990). "Commercial Applications of Ferrofluids." Journal of Magnetism and Magnetic Materials**85**: 233-245.

Raychoudhury, T., et al. (2014). "Straining of polyelectrolyte-stabilized nanoscale zero valent iron particles during transport through granular porous media." Water Research**50**: 80-89.

Ryoo, S., et al. (2012). "Theoretical and experimental investigation of the motion of multiphase fluids containing paramagnetic nanoparticles in porous media."Journal of Petroleum Science and Engineering**81**: 129-144.

Sajith, V., et al. (2010). "Experimental Investigations on the Effects of Cerium Oxide Nanoparticle Fuel Additives on Biodiesel." Advances in Mechanical Engineering Article ID 581407.

Sasidharan, S., et al. (2017). "Temperature dependency of virus and nanoparticle transport and retention in saturated porous media." Journal of Contaminant Hydrology**196**: 10-20.

Sershen, S.R., et al., (2000). "Temperature-sensitive polymer-nanoshell composite for photothermally modulated drug delivery." Journal of Biomedical Matter**51**: 293-298.

Sheng, James. (2011). Modern Chemical Enhanced Oil Recovery: Theory and Practice.

Sposito, G. (2008). The Chemistry of Soils. 2nd Ed. Oxford University Press, New York.

Teja, A. S. and P. Y. Koh (2009). "Synthesis, properties, and applications of magnetic iron oxide nanoparticles." Progress in Crystal Growth and Characterization of Materials**55**: 22-45.

Thomas, C., et al. (2012). Documentation of AEC Standards including the Stim-Lab AEC Standard Core Flood test, Advanced Energy Consortium: 11.

Torkzaban, S., et al. (2012). "Impacts of bridging complexation on the transport of surface-modified nanoparticles in saturated sand." Journal of Contaminant Hydrology. **136-137**: 86-95.

Van Genuchten, M.T. (1980). "A Closed-form Equation for Predicting the Hydraulic Conductivity of Unsaturated Soils." Soil Science Society of America Journal**44**(5): 892-898.

Verwey, E.J., et al., (1948). "Theory of the Stability of Lymphobic Colloids." Elsevier, Amsterdam.

Villamizar, L. C., et al., (2010). "Interfacially Active SWNT/Silica Nanohybrid Used In Enhanced Oil Recovery."Society of Petroleum Engineers

Wang, Y.-X. J., et al. (2001). "Superparamagnetic iron oxide contrast agents: physiochemical characteristics and applications in MR imaging." European Radiology**11**: 2319-2331.

Wang Yl, et al. (2008). "Influence of Electrolyte Species and Concentration on the Aggregation and Transport of Fullerene Nanoparticles in Quartz Sands." Nanomaterials in the Environment**27**(9): 1860-1867.

Xu, S.P., et al., (2006). "Straining of colloidal particles in saturated porous media." Water Resources**42**(12).

Xue, Z., et al. (2014). "Effect of Grafted Copolymer Composition on Iron Oxide Nanoparticle Stability and Transport in Porous Media at High Salinity." Energy and Fuels**28**: 3655-3665.

Yu, H., et al. (2014). "Transport and retention of aqueous dispersions of superparamagnetic nanoparticles in sandstone." Journal of Petroleum Science and Engineering**116**: 115-123.

Zhang, T., et al. (2010). SPE 129885: Nanoparticle-stabilized emulsions for applications in enhanced oil recovery.Society of Petroleum Engineers.